Injured SSTR2^{+} nociceptor axons in neuromas drive chronic spontaneous neuropathic pain

Xiangsunze Zeng[1,2], Rosa I. Martinez-Garcia[2], Shamsuddin A. Bhuiyan[3], Keunjung Heo[1,2], Natalie MacKinnon-Booth[1], Elke Bentley[1], Emily Shea[1], Kangling Wu[4], Omer Barkai[1,2], Bruna Lenfers Turnes[1,2], Selwyn S. Jayakar[1,2], Barbara Gomez-Eslava[1], Mustafa Q. Hameed[1], Celine Santiago[2], Karina Lezgiyeva[2], Emmanuella Osei-Asante[2], Ivan Furfaro[4], Alexander Rotenberg[1], Benjamin R. Johnston[5], Brian J. Wainger[6,7], William Renthal[3], Stéphanie P. Lacour[4], David D. Ginty[2,8]*, Clifford J. Woolf[1,2]*

[1]F.M. Kirby Neurobiology Center, Boston Children's Hospital, Boston, MA, USA

[2]Department of Neurobiology, Harvard Medical School, Boston, MA, USA

[3]Department of Neurology, Brigham and Women's Hospital and Harvard Medical School, Boston, MA, USA

[4]Laboratory for Soft Bioelectronic Interfaces (LSBI), Neuro-X Institute, École Polytechnique Fédérale de Lausanne, Geneva, Switzerland

[5]Department of Neurosurgery, Mass General Brigham, and Harvard Medical School, Boston, Massachusetts, USA

[6]Departments of Anesthesia, Critical Care & Pain Medicine and Neurology, Massachusetts General Hospital, and Harvard Medical School, Boston, Massachusetts, USA

[7]Broad Institute of MIT and Harvard, Cambridge, MA, USA

[8]Howard Hughes Medical Institute, Boston, MA, USA

*Corresponding author. Email:

david_ginty@hms.harvard.edu (D.D.G);

clifford.woolf@childrens.harvard.edu (C.J.W.)

Abstract

Spontaneous pain is a very common but poorly understood consequence of peripheral nerve injury. We developed a system for measuring spontaneous pain-related behaviors in mice over months, which revealed that limb flicks—emerging predominantly 2 months post-injury—reflect spontaneous pain, and that neuromas are the drivers of this component of neuropathic pain. *In vivo* dorsal root ganglion imaging showed that small-diameter sensory neurons are the source of spontaneous ectopic neuroma activity and are different from the intact neurons that drive stimulus-evoked pain. Cell–specific optogenetic stimulation studies identified that injured SSTR2^{+} sensory axons in neuromas are the triggers of spontaneous limb flicks/neuropathic pain. These findings reveal the mechanisms of spontaneous neuropathic pain and open new therapeutic opportunities.

Introduction

Peripheral nerve injury is a major cause of chronic neuropathic pain, resulting in persistent suffering and disability. Spontaneous pain is among the most common and debilitating clinical features of neuropathic pain (*1-3*), yet its underlying mechanisms remain largely unknown. Most preclinical research emphasizes stimulus-evoked withdrawal responses (*4*), which poorly captures the chronic and fluctuating nature of spontaneous pain. This knowledge gap stems from the fact that spontaneous pain arises sporadically and unpredictably, posing challenges for comprehensive quantitative investigations (*5*) and mechanistic discovery.

Existing measures of spontaneous pain are inadequate. For example, the grimace scale performs well in acute pain settings but not for neuropathic pain (*6*). Conditioned

place preference can indicate ongoing pain (*7*), but fails to capture the paroxysmal pain that is a hallmark in patients with peripheral nerve trauma who develop neuromas (*8*). Consequently, studies have relied on intermittent pain-like behaviors such as paw biting or guarding to infer spontaneous paroxysmal pain after nerve injury (*9, 10*). These measures, however, typically depend on short-term video observations and do not provide a comprehensive view of sporadic and unpredictable pain episodes over prolonged periods.

Neuropathic pain research has predominantly centered on acute and subacute post-nerve injury periods (e.g., 1–4 weeks), leaving its chronic features relatively underexplored, even though this is a major clinical issue. Furthermore, the cellular sources of aberrant activity are unclear: early electrophysiological studies demonstrated that both injured and neighboring uninjured sensory fibers generate ectopic discharges soon after axotomy (*10-12*), but the genetically-defined sensory subtypes that drive chronic spontaneous neuropathic pain have not been identified. Finally, a longstanding clinical puzzle is why patients with comparable peripheral nerve insults experience different outcomes, with some developing severe chronic pain while others have moderate or no pain (*13-15*). Although risk factors—genetic predisposition, psychosocial context, prior injury, age, and sex—have been proposed (*13, 16*), the cellular and molecular bases for this variability are still elusive.

By integrating long-term home-cage behavioral studies, *in vivo* calcium imaging, cell-type–specific optogenetic manipulations, and transcriptomic profiling in mice, we now identify that injured SSTR2-expressing (SSTR2^{+}) sensory fibers are the drivers of chronic spontaneous neuropathic pain in animals with painful neuromas.

Results

Painful neuromas drive chronic spontaneous pain after peripheral nerve injury

We began by analyzing defined spontaneous behaviors in mice using a machine-learning–based platform (*17*) following different types of sciatic nerve injury, assessing spontaneous behaviors including guarding, biting/licking, scratching, rearing, and grooming behaviors weekly for up to two months (fig. S1, A and B). All of these behaviors remained unchanged post injury, except for guarding, in which mice lift and hold the paw on the same side as the nerve injury, which increased relative to sham controls from one week after the injury (fig. S1C), in line with previous studies (*9, 10*).

However, we observed an additional and unexpected behavior that was very rare in the first 4 weeks after the nerve injury, but then progressively increased, becoming most prominent at 8 weeks post-injury across all the nerve transection injury models (fig. S1D). We termed this injury-induced behavior a "limb flick", as it is characterized by a stereotyped pattern of rapid, repetitive hindlimb shaking (movie S1). The incidence of limb flicks scaled with injury severity, being most pronounced after a full sciatic nerve transection (SNT), intermediate in the spared nerve injury (SNI) model, where the common peroneal and tibial nerves are injured and the sural nerve remains intact (fig. S1D). Limb flicks were also observed after a sural nerve transection (SuNT) (fig. S1D), which involves only sensory fibers (*18*) and were suppressed by gabapentin (fig. S2A), indicating that this behavior very likely reflects pain and not motor dysfunction. By contrast, limb flicks were absent in acute nociceptive or inflammatory pain models (fig. S2B). These observations suggest that spontaneous limb flicks arise from chronic pathological changes in injured sensory nerve fibers.

Because the limb flick is a chronic pain-related behavior that emerged most robustly in the SNT model, we focused on this nerve injury model for subsequent analyses. To move beyond conventional short-term measures, we established a quantitative framework for long-term home-cage monitoring. Given the stereotyped high-frequency muscle activity underlying limb flicks, we implemented a wireless electromyography (EMG) system with electrodes in the vastus lateralis, the largest quadriceps muscle, coupled with a video recording, to reliably capture injured hindlimb behaviors over extended periods (Fig. 1A). The EMG system faithfully detected repetitive limb flick oscillations, with an average peak frequency of ~13 Hz and most events lasting <1 second (fig. S3, A to C and movie S2), without any apparent motor impairment from the recording electrode implantation (fig. S3D). To determine whether prolonged monitoring reduces behavior variability, we performed a continuous 24-hour recording at 8 weeks post-SNT and assessed intra-animal variation by binning the data into time windows of increasing length. As window size increased, variability progressively declined, but extending the recording period up to 48 hours did not yield a further reduction, when compared with 24 hours (Fig. 1B). These results demonstrate that 24-hour monitoring provides a stable measure of limb flicks and also indicate a circadian component to spontaneous neuropathic pain (*19*).

Using 24-hour recordings, we tracked limb flicks longitudinally. Group averages rose gradually, reaching a peak around 8 weeks post-SNT and remaining at a plateau thereafter, with most increases occurring during the dark phase (7 p.m.–7 a.m.) (Fig. 1, C and D). Between mice, the flick prevalence varied, some mice displayed dramatic increases, whereas others remained at moderate or low levels throughout all time points examined (Fig. 1D). Unlike the intra-animal variability attributable to recording length, this

inter-animal variability likely reflects biological differences and is reminiscent of the different pain phenotypes in patients who develop painful or non-painful neuromas after peripheral nerve injury or an amputation (*14, 15*). Histology confirmed the formation of terminal neuromas proximal to the nerve transection, appearing as bulbous structures filled with exuberant but disorganized axons within fibrotic tissue by 8 weeks post-SNT (Fig. 1E), as described previously (*20*). To test whether the neuromas trigger the limb flicks, we used a transcutaneous poke test, analogous to the clinical Tinel sign evoked by gentle tapping the skin over a peripheral nerve (*21*). Our poke test involved indenting the skin overlying the lesion with a 15 g von Frey filament to mechanically stimulate the underlying neuroma (hereafter referred to as “transcutaneous neuroma poke”). This stimulus increasingly induced limb flicks over time across the nerve injury models, with the strongest responses in SNT, and minimal responses in sham controls or on the side contralateral to SNT (fig. S4A and movie S3). EMG implantation did not affect this outcome (fig. S3E). We assessed flick probability to the transcutaneous neuroma poke in the same mice as used for 24-hour spontaneous flick recordings, which not only revealed comparable inter-animal variability (Fig. 1F), but also demonstrated a strong positive correlation in the chronic phase: mice with more spontaneous flicks were also highly sensitive to the poke test, whereas those with few spontaneous flicks showed little or no flick response to a poke (Fig. 1G). To test causality, we injected lidocaine locally at the neuroma site, a standard clinical intervention (*22*). This virtually abolished the poke-induced flicks in mice with a high pain behavior. In addition, it markedly reduced spontaneous flicks (Fig. 1H), indicating that activity originating in neuromas is the major driver of this chronic spontaneous pain behavior.

To quantify the incidence of the high-pain phenotype, we performed the transcutaneous neuroma poke test in 144 mice at 8–12 weeks post-SNT. Thirty-two percent exhibited a high response probability (≥0.7; hereafter referred to as high-pain), twenty-seven percent exhibited low probability (≤0.3; low-pain), and forty-one percent displayed an intermediate pain phenotype (0.4–0.6; medium-pain), with no sex differences or correlation with the neuroma size (fig. S4, B and C). Finally, neither the poke-induced nor the spontaneous limb flicks required the mechanosensitive channel Piezo2, as evaluated in Piezo2 conditional knockout mice (fig. S5).

Small-diameter sensory axons underpin ectopic activity arising from neuromas

To investigate the neuronal basis of the peripheral ectopic activity, we performed *in vivo* calcium imaging from the L4 dorsal root ganglia (DRG) in 8–12 weeks post-SNT mice using *Vglut2*^{Cre}*::GCaMP6f*, which labels primary sensory neurons across all subtypes. The neuroma or contralateral intact nerve was surgically exposed to allow direct stimulation with von Frey filaments of varying force (Fig. 2A). Poking neuromas induced calcium responses almost exclusively in small-diameter neurons (<25 μm soma diameter), whereas stimulation of the contralateral intact nerve rarely activated neurons of any size (Fig. 2, B and C; and movie S4), with 1.4 g producing the most discriminating response (largest effect size determined by Cohen's d). Neuroma responses also varied across animals: the response amplitude of small-diameter neurons induced by a 1.4 g stimulation differed substantially across mice and was positively correlated with their behavioral pain responsiveness assessed by transcutaneous neuroma poke immediately prior to imaging

(Fig. 2D), supporting a peripheral contribution to the differential pain outcomes in individual mice.

We next assessed spontaneous activity in the same DRG and found that the ipsilateral L4 DRG contained more spontaneously active cells than the contralateral one, specifically within the small-diameter population (Fig. 2E). Mapping these neurons onto those responsive to a neuroma poke showed that the majority—both spontaneously active and those responsive to a poke—were small-diameter neurons (Fig. 2, F and G). Topical lidocaine applied directly at the neuroma largely abolished the spontaneous activity (Fig. 2H), demonstrating that its origin is in the neuroma rather than the DRG. These findings establish injured small-diameter sensory axons as the principal source of ectopic activity, and the likely drivers of spontaneous neuropathic pain.

Pain arising from injured vs uninjured fibers requires distinct sensory cell types

Peripheral nerve injury induces ectopic activity in both injured and adjacent uninjured fibers across different sensory neuron subtypes (*10-12*). We next asked whether activity originating from injured fibers in neuromas and uninjured fibers jointly contribute to a common pain phenotype or act through distinct mechanisms. Because the entire sciatic nerve is severed in the SNT model, we assessed mechanosensitivity of the medial plantar paw which is innervated by the intact saphenous nerve (*23*). Tactile allodynia emerged 4 weeks post-SNT (Fig. 3A), well before spontaneous limb flicks became prevalent. No correlation was found between the intact saphenous nerve-evoked pain and neuroma pain intensity (Fig. 3B), pointing to independent mechanisms. Direct imaging of DRG activity confirmed this separation: completely distinct populations of sensory neurons

were engaged in each pain model. Medium- and large-diameter DRG neurons were the primary responders to medial plantar stimulation, whereas small-diameter neurons predominated in the neuroma pain (Fig. 3, C to F; and movie S4). Locally silencing the neuroma or saphenous nerve endings with lidocaine selectively inhibited responses initiated from each region, respectively (Fig. 3, G and H), providing evidence that pain arising from injured and uninjured fibers is initiated through different mechanisms.

SSTR2^{+} sensory fibers in neuromas drive limb flicks

To functionally link small-diameter neuronal activity to the spontaneous pain, we chemogenetically silenced a broad population of Aδ- and C-fiber sensory neurons defined by *Nav1.8^{Cre}* expression, which encompasses most, if not all, small-diameter neurons (*24*). Administration of the DREADD agonist compound 21 (C21) significantly suppressed both spontaneous and poke-induced limb flicks in high-pain *Nav1.8^{Cre}::hM4Di* mice but not in littermate controls (Fig. 4A), indicating that activity from small-diameter neurons is necessary for pain behavior.

Transcriptomic studies have identified at least 16 genetically distinct DRG sensory subtypes (*25, 26*) with unique physiology and morphology (*26*). We performed single-nucleus RNA sequencing (snRNA-seq) of DRG from mice 10 weeks post-SNT and confirmed the presence of all these cell types in both high- and low-pain conditions (Fig. 4C and fig. S6A). To identify specific sensory subtypes whose activation may drive the limb flicks, we conducted an optogenetic gain-of-function screen, using transgenic mouse lines that collectively encompass all sensory subtypes with somatic diameters <25 μm (*26*). Because neuromas reside deep within fibrotic tissue, we adapted a miniaturized LED

cuff (*27*) for localized epineural activation of sensory axons either in neuromas or contralateral intact nerves (Fig. 4B and fig. S7). In mice expressing opsins in the C-Heat (SSTR2$^+$) subtype (*Sstr2*$^{T2a\text{-}CreER}$*;Calca-FlpE;R26*$^{LSL\text{-}FSF\text{-}ReaChR::mCitrine}$), a single 10-ms 470-nm pulse delivered to a neuroma induced limb flicks and, to a lesser extent, other pain-related behaviors (vocalization, jump, licking, and avoidance either individually or in combination) (*5*), with significantly lower activation thresholds than for contralateral intact nerves (Fig. 4, D and E). By contrast, Aδ-high-threshold mechanoreceptors (HTMR)/Heat (SMR2$^+$) neurons elicited behavioral responses when intact nerves were stimulated but rarely when neuromas were activated (Fig. 4, D and E). This discrepancy likely reflects the preferential loss of SMR2$^+$ axons in neuromas (fig. S8). Other subtypes showed little or no nocifensive output: activating Aδ-low-threshold mechanoreceptors (Aδ-LTMRs), C-LTMRs, or C-HTMR/Heat (CYSLTR2$^+$/SST$^+$) neurons produced no consistent behaviors from either neuromas or intact nerves, whereas stimulating C-HTMR/Heat (MRGPRA3$^+$), C-HTMR/Heat (MRGPRB4$^+$), C-HTMR/HEAT (MRGPRD$^+$), C-Cold (TRPM8$^+$) axons with strong optical power occasionally evoked avoidance, guarding, or licking behaviors from either site, but rarely induced limb flicks (Fig. 4, D and E; and movie S5).

Anatomical analyses revealed denser SSTR2$^+$ fibers in neuromas than contralateral intact nerves, but a reduced presence of SMR2$^+$, MRGPRA3$^+$, and MRGPRD$^+$ nerve fibers, with MRGPRD$^+$ axons almost completely absent (fig. S8), likely reflecting cell death in this population after peripheral nerve trauma (*28*).

Because activation of SSTR2$^+$ sensory axons robustly induced limb flicks, we further characterized how their activity relates to different pain-related behaviors and response dynamics. High-frequency or prolonged optogenetic stimulation did not change the

incidence of limb flicks or other behaviors, except audible vocalizing—a response uniquely triggered by SSTR2$^+$ activation—showed an increased occurrence under these conditions, suggesting a dependence on summation of activity (Fig. 4F, left). Response latency analyses showed that limb flicks occurred with an average latency of 259 ms, longer than a jump or avoidance response, but well before self-licking, which was markedly delayed (Fig. 4F, middle), suggesting that limb flicks capture pain reactions on a time scale quite distinct from withdrawal reflexes. Lastly, we noted from snRNA-seq that *Scn10a* (encoding voltage-gated sodium channel $Na_v1.8$) and *Scn3a* ($Na_v1.3$) were selectively upregulated in the SSTR2$^+$ subtype under high-pain conditions (fig. S6, B and C), suggesting a contribution to hyperexcitability of this population in painful neuromas. To test this directly, we analyzed the stimulation strength required to induce limb flicks in high-, medium-, and low-pain mice. A Cox proportional hazards model with optical power as the time scale and flick to optogenetic stimulation as the event, revealed that the flick probability determined by the transcutaneous neuroma poke test significantly predicted optogenetic threshold (*hazard ratio* = *198.8*, $p = 0.0023$), indicating that high-pain mice flick at a lower optical power, whereas low-pain mice require a higher power to elicit flicks (Fig. 4F, right).

These findings demonstrate that injured SSTR2$^+$ sensory axons become hypersensitive in painful neuromas and drive chronic spontaneous limb flick pain behavior.

Discussion

The mechanisms of spontaneous pain have remained obscure largely because of the lack of reliable measures. Here we establish a long-term recording platform that identifies limb flicks as a robust behavioral readout of chronic spontaneous pain and trace its origin to injured SSTR2$^+$ axons in painful neuromas. These findings, by linking a reproducible behavioral measure of spontaneous pain to an underlying neural mechanism, open new avenues for mechanistic studies and therapeutic discovery.

Spontaneous limb flicks peaking at 2 months represent an objective readout of chronic spontaneous pain in mice after nerve trauma. Quantifying flicks over 24 hours lowers variability and provides a window into spontaneous events that are sparsely sampled with short recording sessions. Long-term tracking of DRG neural activity in awake animals (*29*) can now reveal how individual neurons transition from acute to chronic post-injury states (*30*). Extending such longitudinal approaches with clinically validated tools such as EEG and EMG (*31*) may enable the identification of unbiased biomarkers for chronic spontaneous neuropathic pain in patients.

Most preclinical neuropathic pain studies model pain arising from uninjured afferents (*23*), where Aδ/Aβ-LTMRs are rerouted into nociceptive circuits via dorsal-horn plasticity (*30, 32*), with Piezo2-dependent mechanotransduction essential for this mechanical allodynia (*33*). We found that medium/large-diameter uninjured fibers dominate mechanical allodynia, whereas small-diameter injured fibers drive spontaneous neuropathic pain (Fig. 3). Current clinical diagnostic frameworks lump these manifestations under a single “neuropathic pain” label, and treatment guidelines recommend single agents (e.g., gabapentinoids) without delineation of evoked or

spontaneous pain. This likely contributes to variable therapeutic efficacy through a mechanism–therapy mismatch (*34*). Our findings support revisiting diagnostic criteria to explicitly differentiate uninjured-fiber evoked allodynia from injured-fiber triggered spontaneous pain, and develop specific targeted interventions aligned with the dominant driver in each patient.

The neuroma poke mechanical sensitivity occurs independently of Piezo2 (fig. S5). The intrinsically low mechanosensitivity of SSTR2$^+$ neurons under normal physiological conditions (*26*) suggests another transduction mechanism, including the injury-induced hyperexcitability at neuroma terminals. After nerve trauma, perineurial/epineurial disruption exposes axonal sprouts to a stiff, fibrotic matrix, such that minor mechanical perturbation can deform the axolemma and disturb periaxonal ions, producing small depolarizations that Na_v channels amplify. Na_v gating itself is modulated by membrane tension (*35*), providing a potential biophysical route for poke sensitivity without canonical mechanotransducers. This effect would be more likely if Na_v channels ectopically accumulate at a high density by ankyrin scaffolds (*36*), creating a trigger zone at neuroma tips, a scenario supported by our transcriptomic data (fig. S6, B and C) and human neuroma pathology (*37*), and would also explain spontaneous ectopy within the same cells: subthreshold oscillations in a Na_v-enriched microdomain more readily reach threshold, yielding spontaneous firing.

Our findings indicate that injured SSTR2$^+$ sensory axons within neuromas are a primary driver of spontaneous pain and thus a prime interventional target, consistent with clinical practice where local lidocaine application relieves neuroma pain (*22*). However, lidocaine offers only transient, non-selective relief. Two platforms may offer routes for localized,

subtype-focused delivery to neuromas: engineered AAV capsids with enhanced peripheral-neuron tropism, combined with payload strategies that mitigate molecular size constraints to achieve durable transduction in the SSTR2^{+} nociceptors, or lipid nanoparticles for transient, redosable delivery (*38*) that could selectively silence potential molecular drivers such as *Scn10a* and *Scn3a* at the RNA level. Together, these strategies could extinguish pathological ectopy at its source while preserving fundamental sensory functions and minimizing central exposure.

Clinical variability in pain is often attributed to genetic background and life experience (*13, 16*). Despite an experimental design with essentially identical nerve injury, genotype, and environment, our model produced divergent high- and low-pain neuromas, implicating intrinsic stochastic processes in the periphery. In non-linear systems, small stochastic perturbations during an early injury response, in gene expression (*39*), cellular composition (*40*), ion channel gating (*41*), trophic and inflammatory tones (*42*), can steer lesions onto divergent post-injury trajectories (*43*). The formation of painful neuromas may be primed by differential pathological interactions between neurons and non-neuronal cells after injury (*42, 44-48*). Understanding the factors that drive such divergent paths during the subacute transition phase will be key to developing early protective interventions that address the root causes of the pathology (*34*).

Our longitudinal measure reveals a pronounced 24-hour circadian pattern, characterized by increased pain-related behaviors during the dark/active phase. Circadian influences on pain are well-recognized clinically (*19*), but the underlying mechanisms remain poorly defined. Peripheral nerve injury also fragments non-REM sleep (*49*), and sleep deprivation sharpens pain sensitivity (*50*), suggesting a bidirectional

loop between circadian and homeostatic sleep states and pain. These observations highlight the importance of time-of-day, both for studying pain pathophysiology—given that most behavioral assays are performed during the day—and timing of therapeutic interventions.

In conclusion, our findings establish a framework for quantitively measuring chronic spontaneous neuropathic pain and identify the neural cell types, and candidate pathways for future therapeutic interventions, and provides a robust platform for the mechanistic dissection of injured-fiber–driven chronic pain in both the peripheral and central nervous system.

Materials and Methods

Mice

All experiments were conducted in accordance with the guidelines of the Boston Children's Hospital Institutional Animal Care and Use Committee (IACUC) under protocols 00001507 and 00002403, or by the Harvard Medical School IACUC under protocol 00001036. Mice were housed under temperature-controlled conditions on a 12-hour light/dark cycle (lights on at 7:00 a.m., off at 7:00 p.m.) with ad libitum access to food and water. Both male and female mice were used in all experiments. The C57BL/6J strain (JAX #000664; The Jackson Laboratory) was used unless otherwise specified, with transgenic strains detailed in the relevant sections below.

Peripheral nerve injury models

Surgeries were performed on 8–9-week-old mice under aseptic conditions. Anesthesia was induced and maintained with 2% isoflurane (Patterson Veterinary, #07-890-8115) delivered via a nose cone. Throughout the procedure, body temperature was maintained at 37°C using a heated pad to prevent hypothermia. Sciatic nerve injuries were performed using standardized protocols as follows. 1. The surgical site was shaved, and residual hair was completely removed using Nair. The area was then sterilized with 70% ethanol and Betadine. 2. A small skin incision was made over the lateral thigh, above the biceps femoris. The underlying musculature was carefully separated and retracted to expose the sciatic nerve. 3. For sham controls, the sciatic nerve was gently freed from surrounding connective tissue using curved forceps without causing any damage; For SNT injury, a segment of the sciatic nerve trunk 5 mm above the sural, common peroneal, and tibial

nerves was ligated with 6-0 sutures (Ethicon, #K889H) followed by a complete transection proximal to the ligation using microsurgical scissors. An additional 5 mm segment of the distal nerve stump was excised. For SNI injury, the common peroneal and tibial nerve branches were ligated and transected in the same manner, leaving the sural nerve intact. For SuNT injury, the sural nerve branch was ligated and transected in the same manner, leaving the common peroneal and tibial nerve branches intact (fig. S1A). 4. The musculature was then folded back to cover the sciatic nerve with the skin closed with 6-0 sutures. 5. Mice were placed on a 37°C heated pad postoperatively until they fully recovered before being returned to their home cages.

Automated behavioral screening

The recording setup and analytic platform were identical to those previously described (*17*). Briefly, mice were recorded inside a black acrylic enclosure (18 × 18 × 15 cm; length × width × height), which was closed on all sides except for the bottom and positioned on a 25-cm square piece of 5-mm thick glass floor. To ensure consistent illumination from below, two independent 850-nm near-infrared (NIR) LED strips (SMD5050-300-IR, Huake Light Electronics Co., Ltd., Shenzhen, China) were mounted 10 cm beneath the glass floor. These were carefully positioned to prevent reflections from interfering with the recorded images. The LED strips were powered by a 12-V DC power supply. Video recordings were acquired in darkness using an NIR camera (Basler acA2000-50gmNIR GigE, Basler AG, Ahrensburg, Germany) positioned 30 cm below the glass surface. Pylon viewer software (v4.1.0.3660, Basler) was used to capture videos under standardized camera settings. All recordings were conducted at 25 Hz with an initial resolution of 1000

× 1000 pixels, which was subsequently downsized to 500 × 500 pixels for high throughput analysis. For each injury type, four male and four female C57BL6/J mice were used. To minimize stress and ensure natural behavior, mice were habituated for 30 minutes in the recording chamber followed by a 30-minute recording session at each time point (fig. S1, C and D). Only one mouse was placed in the chamber at a time.

To analyze behaviors from the recordings, we used BAREfoot, a supervised machine learning algorithm that integrates pose estimation with light-based measurements of body-part pressure and distance (*17*). For behaviors without pre-existing classifiers, training datasets were generated by manual annotation of videos by experienced scorers, and new classifiers were subsequently trained. The resulting library of trained classifiers enabled automated, frame-by-frame scoring of a behavioral repertoire that included rearing, grooming, scratching, biting/licking, guarding, and limb flicks in freely moving mice (fig. S1).

Home-cage EMG/video recording system

Implantation of wireless telemetry transmitters and recording was performed aseptically in 8-week-old C57BL/6J mice under 2% inhaled isoflurane anesthesia. Wireless telemetry transmitters (PhysioTel ETA-F10; Data Sciences International, St. Paul, MN) were implanted by making a short skin incision along the dorsal aspect of the left hindlimb. A subcutaneous pocket was created by blunt dissection over the back, cephalad to the hindlimb, to house the transmitter body. For EMG recording, a pair of recording and reference electrode leads were stripped of silicone insulation over a 2–3 mm segment, inserted into the vastus lateralis muscle, and secured to the muscle surface with 5-0 nylon sutures to prevent displacement. The incision was closed with surgical staples and tissue

adhesive, and mice were returned to their home cages to recover for ~2 weeks before undergoing the SNT procedure. For experiments shown in Fig. 1, C, D and F, sham controls included 3 males and 2 females, and the SNT group included 6 males and 4 females. Mice in the sham group were also used to assess weight bearing and gait parameters post-implantation (fig. S3D) using a previously reported platform (*51*). In a separate cohort, 3 high-pain and 3 low-pain mice at 8 weeks post-SNT were implanted with transmitters to evaluate the impact of implantation on neuroma pain sensitivity (fig. S3E).

Mice were housed in custom-designed home cages equipped with overhead video cameras with night-vision, maintained under a 12-hour light/12-hour dark cycle (lights on at 7 a.m. and off at 7 p.m.) in temperature- and humidity-controlled chambers, with ad libitum access to food and water (Fig. 1A). In a subset of animals, four additional side-view IP cameras (M1145-L Network Camera, Axis) were used. Video/EMG recordings (sampled at 1000 Hz) were acquired in real time using the DSI Ponemah data acquisition platform (Data Sciences International, St. Paul, MN).

To examine the frequency-domain characteristics of EMG signals representing different behaviors, we performed fast Fourier transform (FFT) analysis on raw EMG time series data with Python's scipy.fft module to determine dominant frequency for each behavior defined by video observations (fig. S3A). The raw amplitude values of the corresponding time series were first transformed into the frequency domain. The resulting spectrum was computed over the range of 0 to 200 Hz. To facilitate comparison across time series and to highlight relative peak frequencies independent of absolute amplitude differences, the FFT magnitude spectrum for each trace was normalized by dividing all frequency

amplitudes by the maximum amplitude within that trace. This rescaled the values to a range between 0 and 1, allowing identification of the dominant frequency peaks while minimizing inter-sample variability in absolute signal strength (Fig. 1B and fig. S3B). Event amplitudes were defined as the absolute peak-to-peak value during each event (fig. S3B). Autocorrelation was computed using the autocorrelation function up to 1000 ms using FFT-based methods. The first positive peak after lag 0 was identified to extract both the dominant periodicity and its autocorrelation strength (fig. S3B). The coefficient of variation was calculated as the ratio of the standard deviation to the mean of event counts at each binned window (fig. S3C).

For scoring limb flicks, raw EMG signals were bandpass filtered at 5–30 Hz. Limb flicks were defined as bouts of repetitive spikes in the filtered EMG trace (fig. S3A and movie S1). Based on features distinguishing limb flicks from other behaviors (fig. S3B), we implemented a two-step semi-manual scoring pipeline. First, EMG traces were screened using a dynamic threshold–based automated spike detection algorithm in NeuroScore CNS Data Analysis Software (v3.6; DSI, Data Sciences International, St. Paul, MN) with broad parameters as follows. Threshold ratio: 1.2; Maximum ratio: 3; Minimum value: 5 μV; minimum spike duration: 1 ms; Maximum spike duration: 1000 ms; Minimum inter-spike interval: 10 ms; Maximum inter-spike interval: 1000 ms; Minimum spike train duration: 10 ms; and Minimum number of spikes: 2. This automated step detected >95% of true-positive events as confirmed in pilot observations. Second, automatically detected events were reviewed by an experimenter blinded to the experimental condition (sham vs. SNT and time point post-surgery), who cross-referenced detection timestamps with simultaneous video recordings to exclude false positives.

Transcutaneous neuroma poke test

Mice were shaved around the thigh area before behavioral assay. Acclimation was conducted over two consecutive days prior to the actual test. During acclimation, mice were placed on a laboratory bench while the investigator gently held their tails. A series of pokes (20–50 repetitive trials covering the entire thigh area, ~15 minutes per mouse) were applied using a 15 g von Frey filament (Stoelting Co, #58011) to familiarize the animals with the testing environment. This acclimation step was crucial, as mice otherwise exhibited escaping behavior in response to mechanical stimulation, even in the absence of injury. Following acclimation, mice typically remained calm and stationary, indicating readiness for the actual behavioral test. If mice continued to display escaping or excessive movements, acclimation was extended until they reached a stable state. Additionally, trials during this acclimation process enabled the investigators to identify a 'target point'—the area on the thigh that elicited the most consistent flicking response. This point often corresponded to the precise location of the neuroma, as later confirmed by post-hoc dissection. In mice that did not exhibit a flicking response throughout acclimation, the 'target point' was set on the skin area directly above the site of the nerve transection.

For the behavioral test, 10 trials of mechanical stimulation were applied to the identified 'target point' using the 15 g von Frey filament, with an inter-stimulus interval of >5 seconds. If a stimulus did not evoke an immediate flicking response, it was maintained for 3 seconds. Trials with no response after this duration were counted as non-responsive (movie S3). Since injured mice sporadically exhibited spontaneous flicking behaviors, any response occurring more than 2 seconds after stimulus offset was not counted, and the

trial was repeated. Occasionally, mice exhibited other behaviors to pokes (e.g., licking or guarding), which were not quantified as they were rare and also occurred on the contralateral side. Flicking probability to poke was quantified as the proportion of trials that elicited flicking behaviors relative to the total number of trials. For animals tested repeatedly on different days, investigators were blinded to their previously assessed pain phenotype.

Plantar von Frey assay

Mice were placed individually in transparent plastic chambers on a wire mesh grid and acclimated to the testing environment for 60 min on two consecutive days. Calibrated von Frey filaments (0.008–4.0 g) were applied to the medial plantar surface (saphenous nerve territory) of the injured side using the Up-Down method (*52*). Testing was performed 1 day before SNT and weekly thereafter up to 8 weeks post-SNT, and 50% withdrawal thresholds were calculated (Fig. 3A).

For plantar von Frey testing in Piezo2 conditional knockout mice generated from *Cdx2*^{Cre} (JAX #009350) (*53*), *Piezo2*^{flox} (JAX #027720) and *Piezo2*$^{flox/Null}$ strains (*54*), the contralateral central plantar area was targeted using the same Up-Down method (fig. S5).

Drug treatments

For the drug-related tests, spontaneous behavioral assessments were performed in the black box recording system for 30 min rather than in the home-cage monitoring setup, as the effective window of drug action is on the scale of hours. To mitigate intra-animal variability and ensure robust statistical power, a larger sample size was included.

Gabapentin (Medisca, #60142-96-3) was administered intraperitoneally at 30 mg/kg. Spontaneous behaviors were recorded in the black box for 30 min before injection (pre) and again for 30–60 min post-injection (fig. S2A). Compound 21 (Hello Bio, #HB4888) was administered intraperitoneally at 3 mg/kg to mice carrying either the hM4Di allele (B6.129-*Gt(ROSA)26Sor*$^{tm1(CAG\text{-}CHRM4*,\text{-}mCitrine)Ute}$/J; JAX #026219) alone or hM4Di under the control of *Nav1.8*^{Cre} (B6.129(Cg)-*Scn10a*$^{tm2(cre)Jwo}$/TjpJ; JAX #036564) (*24*). Spontaneous behaviors were recorded for 30 min before injection (pre) and for 30–60 min post-injection, followed by transcutaneous neuroma poke tests conducted 60–70 min post-injection (Fig. 4A). 50 µl 1% lidocaine hydrochloride monohydrate (Sigma-Aldrich, #L5647) was administered via deep intramuscular–perineural injection around the lateral upper thigh where the neuroma resides. Spontaneous behaviors were recorded for 30 min beginning 15 min after injection, immediately followed by transcutaneous neuroma poke tests conducted 45–55 min post-injection (Fig. 1H). For calcium imaging experiments, 10 µL of 1% lidocaine hydrochloride monohydrate was applied either topically to surgically exposed neuromas (Fig. 2H and Fig. 3G) or via intraplantar injection (Fig. 3H), and von Frey assessments were performed 5 min after administration. Capsaicin (Sigma-Aldrich, #M2028), zymosan (Sigma-Aldrich, #Z4250), and CFA (Sigma-Aldrich, #F5881) were administered as described in the legend to fig. S2B. Spontaneous limb flicks and paw biting/licking behaviors were manually counted by investigators blinded to treatment.

In vivo imaging of DRG activity

DRG imaging was performed as described previously (*30*). Mice carrying both *Vglut2-ires-Cre* (B6J.129S6(FVB)-*Slc17a6*$^{tm2(cre)Lowl}$/MwarJ; JAX #28863) and *Ai95D* (B6J.Cg-*Gt(ROSA)26Sor*$^{tm95.1(CAG-GCaMP6f)Hze}$/MwarJ; JAX #028865) alleles were used for imaging at 8–12 weeks post-SNT. Anesthesia was induced with 2.5% isoflurane and maintained at 2% via a nose cone. Mice were placed on a heated pad to maintain the body temperature at 37 °C, and ophthalmic ointment was applied to the eyes throughout the surgery and imaging. The back was shaved, and a rectangular incision was made between the lumbar enlargement and pelvic bone with the skin folded away. A dorsal laminectomy was performed in four steps. First, a 1.5-cm midline incision caudal to the lumbar enlargement area was made to create space for clamping. Second, a 3-4 mm incision was made approximately 1 cm rostral to the pelvic bone to expose the spine where the L4 DRG is situated. Third, muscles and connective tissues were removed with scissors and forceps. Fourth, the L4 transverse process was excised using rongeurs, and small vertebral fragments were carefully trimmed with fine forceps to fully expose the DRG. Bleeding was controlled using absorbent paper points (Electron Microscopy Sciences, #71011-01). To minimize motion artifacts from respiration, a custom spinal clamp (*26*) was used to secure the spine over the vertebrae 5 mm rostral to the L4 DRG. Illumination was provided with a collimated 470 nm light-emitting diode through a 10x, 0.3 numerical aperture air objective. The clamp was adjusted to ensure the DRG surface was as level as possible, visualizing the maximum surface area in the focal plane, typically covering ~80% of the entire DRG. A single focal plane was selected for each animal based on the presence of neurons exhibiting robust calcium responses to indentation of the medial hindpaw (saphenous nerve territory). A 30-minute imaging session without

external stimulation was conducted to assess spontaneous activity. The neuroma was then surgically exposed following a procedure similar to sciatic nerve exposure during SNT injury. Mechanical stimuli of varying forces were applied to the neuroma using von Frey filaments. Each force was delivered in five trials, with an interstimulus interval of >5 seconds. After imaging the ipsilateral L4 DRG, the same procedure was repeated for the contralateral L4 DRG, except that mechanical stimuli were applied to the intact sciatic nerve at a location corresponding to the neuroma site on the ipsilateral side. The imaging order (i.e., ipsilateral or contralateral first) was randomized to minimize potential variability due to anesthesia duration. Images were acquired at 10 Hz with a 99 ms exposure time during neuroma stimulation. The stimulation was also recorded simultaneously at 25–30 Hz using a digital camera, with the video output time-stamped to synchronize with GCaMP imaging data. For imaging spontaneous activity, exposure time was reduced to 35 ms to minimize photobleaching during long-term recordings. Isoflurane concentration was reduced to 1% throughout the imaging process.

Imaging data were analyzed using the open-source CaImAn package (*55*). Briefly, data were first corrected for motion using the NoRMCorre algorithm. Regions of interest (ROIs) were identified using a constrained non-negative matrix factorization (CNMF) framework, which jointly estimates spatial footprints and temporal activity traces. Extracted fluorescence traces were detrended to correct for bleaching and converted to ΔF/F on a per-cell basis, with baseline (F) defined as the average of the lowest 10% of fluorescence values. Automatically extracted ROIs were reviewed by an investigator to correct false positives and false negatives. The corresponding calcium traces were then evaluated against quality criteria, including spatial correlation, temporal signal-to-noise ratio (ΔF/F

exceeding 3× the standard deviation of baseline fluctuation for ≥0.5 s), appropriate rise and decay kinetics, and consistent morphology. Only ROIs meeting these criteria were retained for analysis.

To classify spontaneously active cells, neuroma poke–responsive cells, and dual-active cells based on calcium activity, we used an unsupervised clustering approach with Gaussian Mixture Models (GMMs) implemented in Python's scikit-learn package. The model estimated the probability of each cell belonging to one of three classes (Fig. 2G) or two classes (Fig. 3D) according to its peak ΔF/F across the corresponding imaging sessions, with final cluster assignment determined by maximum posterior probability (decision boundary).

Miniaturized LED cuff and epineural optogenetic activation

We adapted a previously developed wireless LED array (*27*) into a wired device to enable behavioral screening across multiple Cre lines (Fig. 4B and fig. S7). The fabrication process for the LED cuff began with the spin-coating of a 3 μm-thick polyimide (PI) layer (HD Microsystems GmbH, catalog no. PI2611) onto a silicon (Si) wafer coated with an aluminum (Al) layer. The underlying Al acted as a sacrificial layer for subsequent device release. The PI was then baked at 300 °C for 2 hours to complete the imidization process. A 130 nm-thick silicon carbide (SiC) layer was then deposited via plasma-enhanced chemical vapor deposition (PECVD) using an Oxford PlasmaLab System 100 under the following conditions: 133 sccm Ar, 60 sccm CH_4, and 375 sccm of 2% SiH_4 in Ar; RF power of 25 W; substrate temperature of 300 °C; and deposition time of 10 minutes. Next, a metal stack composed of Titanium/Platinum/Gold/Platinum/Titanium (Ti/Pt/Au/Pt/Ti,

thicknesses: 10/10/200/10/10 nm) was sputtered using an AC450 system (Alliance-Concept) and patterned by lift-off in an ultrasonic acetone bath (80 kHz, 100% power, 10 minutes). A second 130 nm SiC layer was deposited, followed by spin-coating and baking of an additional PI layer using the same parameters as before. A Titanium/Silicon Oxides (Ti/SiO_2) bilayer (10/25 nm) was subsequently sputtered onto the top PI surface. The final device patterning was carried out using an ICP-RIE etch system (Corial 210IL), defining the shape of the cuff and opening windows for LED integration and soldering.

Following the microfabrication steps, solder paste bumps (~50 μm diameter, Chipquik, catalog no. SMDLTLFP10T5) were manually deposited onto the exposed contact pads. Micro-LEDs (Cree Inc., catalog no. DA2432) were placed using a pick-and-place system (JFP Microtechnic) and bonded by heating the wafer on a hotplate at 165 °C, ensuring both electrical and mechanical connections. To improve hermetic sealing, a 15 wt% solution of poly(isobutylene) (PIB, Oppanol, BASF) in cyclohexane (Sigma-Aldrich) was applied to the die surface via pneumatic dispensing. Finally, a 60 μm-thick encapsulating layer of polydimethylsiloxane (PDMS) was printed, baked at 70 °C for 12 hours, and patterned by blade cutting. DC voltage was measured using a source meter (Keithley 2400) while sweeping the input current from 0.5 to 17 mA. Simultaneously, the total optical power output at 470 nm was measured using a calibrated photodiode (S170C, Thorlabs) connected to a power meter console (PM100D, Thorlabs). During measurements, the distance between the photodiode and the micro-LEDs was maintained at approximately 1 mm.

The neuroma or intact sciatic nerve was exposed as described in the sciatic nerve injury procedure. The LED cuff was positioned beneath the neuroma or intact sciatic nerve

at a perpendicular angle, and its distal end was folded 180° to wrap around the target site. This configuration placed one set of LEDs on the front and the other on the back of the neuroma or nerve (Fig. 4B, right). To secure the device, the two proximal anchoring points were sutured to each other and to the adjacent proximal muscles, while the distal anchoring points were sutured to the upper thigh muscle for additional stabilization (Fig. 4B, right). 10-0 sutures (Ethicon, #2794G) were used for these anchoring sites. The wires with a female nano-miniature circular connector (Omnetics, #A79103-001) were routed subcutaneously to the backside, where a small skin pocket was created to externalize the connector. The thigh incision was closed using 6-0 sutures, while the skin pocket was sealed with tissue adhesive (3M Vetbond, #1469). After each experiment, the placement of the LEDs was confirmed. If displacement occurred (e.g., slippage from the neuroma), the animal was excluded from analysis.

The following transgenic lines were used to target sensory neuron subtypes: *Sstr2*$^{T2a\text{-}CreER}$*;Calca-FlpE;R26*$^{LSL\text{-}FSF\text{-}ReaChR::mCitrine}$ for the C-Heat (SSTR2^{+}) subtype, *Mrgprd*^{CreER}*;R26*$^{LSL\text{-}ReaChR::mCitrine}$ for the C-HTMR/HEAT (MRGPRD^{+}) subtype, *Th*$^{T2a\text{-}CreER}$*;Avil*^{FlpO}*;R26*$^{LSL\text{-}FSF\text{-}ReaChR::mCitrine}$ for the C-LTMR subtype, *Smr2*$^{T2a\text{-}Cre}$*;Calca-FlpE;R26*$^{LSL\text{-}FSF\text{-}ReaChR::mCitrine}$ for the Aδ-HTMR/Heat (SMR2^{+}) subtype, *TrkB*^{CreER}*;Avil*^{FlpO}*; R26*$^{LSL\text{-}FSF\text{-}ReaChR::mCitrine}$ for the Aδ-LTMR subtype, *Mrgpra3*^{Cre}*;R26*$^{LSL\text{-}ReaChR::mCitrine}$ for the C-HTMR/Heat (MRGPRA3^{+}) subtype, *Mrgprb4*^{Cre}*;R26*$^{LSL\text{-}ReaChR::mCitrine}$ for the C-HTMR/Heat (MRGPRB4^{+}) subtype, *Cysltr2*^{Cre}*;R26*$^{LSL\text{-}ReaChR::mCitrine}$ for the C-HTMR/Heat (CYSLTR2^{+}/SST^{+}) subtype, *Trpm8*$^{T2a\text{-}FlpO}$*; R26*$^{FSF\text{-}ReaChR::mCitrine}$ for the C-Cold (TRPM8^{+}) subtype. All the mouse lines used to generate these genetic crosses have been previously described: *Sstr2*$^{T2a\text{-}CreER}$ (JAX #039563) (*26*), *Mrgprd*^{CreER} (JAX #031286) (*56*), *Th*$^{T2a\text{-}CreER}$

(JAX #025614) (*57*), *Smr2*$^{T2a\text{-}Cre}$ (JAX #039562) (*26*), *TrkB*^{CreER} (JAX #027214) (*58*), *Mrgpra3*^{Cre} *(59)*, *Mrgprb4*^{Cre} (*60*), *Cysltr2*^{Cre} (JAX #039985) (*26*), *Trpm8*$^{T2a\text{-}FlpO}$ (JAX #039564 (*26*), *Calca-FlpE (61)*, *Avil*^{FlpO} *(61)*, *R26*$^{LSL\text{-}FSF\text{-}ReaChR::mCitrine}$ (JAX #024846), *R26*$^{LSL\text{-}ReaChR::mCitrine}$ (JAX #026294), *R26*$^{FSF\text{-}ReaChR::mCitrine}$ (derived from JAX #024846 by germline excision of LSL cassette). All transgenic mouse lines were maintained on a mixed background and included males and females. CreER lines were induced by a single intraperitoneal injection of tamoxifen dissolved in sunflower seed oil, prepared as previously described (*26*). For *Sstr2*$^{T2a\text{-}CreER}$*; Calca-FlpE; R26*$^{LSL\text{-}FSF\text{-}ReaChR::mCitrine}$, we administered 3 mg of tamoxifen at 3 weeks; *Mrgprd*^{CreER}*;R26*$^{LSL\text{-}ReaChR::mCitrine}$, 2 mg at 3-4 weeks; *Th*$^{T2a\text{-}CreER}$*;Avil*^{FlpO}*;R26*$^{LSL\text{-}FSF\text{-}ReaChR::mCitrine}$, 2 mg at 3-6 weeks; *TrkB*^{CreER}*; Avil*^{FlpO}*; R26*$^{LSL\text{-}FSF\text{-}ReaChR::mCitrine}$, 0.5 mg at postnatal day 3 to day 5.

For optogenetic activation, the external connector was coupled to an adapter linked to a stimulator (AM-Systems, Grass Instruments S88). When mice were in a calm, awake state, a single 10 ms pulse was delivered at various voltages corresponding to different optical power levels with behaviors recorded by a high-speed camera at 120 Hz. Each power level was tested in 10 trials with an inter-stimulus interval of >1 min. Behaviors occurring during stimulation or within 2 s after stimulus offset were counted as positive responses. Response probability was calculated as the proportion of trials with a behavioral response out of 10 trials for each animal (Fig. 4D). The occurrence rate of each behavior type was calculated as the number of trials in which that behavior was induced from the ipsilateral neuroma site at 60 mW across all animals, divided by the total number of trials (i.e., 10 × number of animals) (Fig. 4D). Response latency (Fig. 4F, middle) was defined as the time between opto-stimulation onset (single 10 ms pulse at

60 mW) and the initiation of the behavior. Single 10 ms pulses were used for all optogenetic experiments except in Fig. 4F left panel, where repetitive 10 ms pulses at 10 Hz or continuous light (60 mW) were delivered for 5 s. Cre expression in all animals was verified *post hoc* by histological analysis following completion of optogenetic experiments.

Survival analysis using the Cox proportional hazards regression model was used to determine whether flick probability to transcutaneous neuroma pokes predicted the optical threshold for evoked limb flicks. Optical power (mW) was treated as the time-to-event variable, and the first limb flick to optogenetic stimulation was defined as the event. Animals that did not flick at the maximum tested power (60 mW) were right-censored. Von Frey flick probability (0–1) was included as a continuous covariate. Hazard ratios with 95% confidence intervals were reported, and significance was assessed using the likelihood-ratio test (Fig. 4F, right).

Histology

Neuromas, contralateral intact sciatic nerves, or DRG were fixed in 4% paraformaldehyde (PFA) in PBS at 4 °C overnight. Nerves were cryoprotected in 30% sucrose in PBS at 4 °C for one to two days, embedded in OCT compound (Sakura Finetek) on dry ice, and cryosectioned longitudinally (parallel to the axon trajectory) at 50 μm. DRG were fixed and processed for whole-mount staining. Sections or whole DRG were permeabilized in 1% Triton X-100 in PBS for 20 min and blocked in 10% normal donkey with 0.3% Triton X-100 in PBS overnight at 4 °C. Primary antibody incubation was performed overnight at 4 °C in blocking solution (1:500) using anti-GFP (Thermo Fisher, #A10262) and anti-PGP9.5 (Abcam, #ab108986). Secondary antibodies were incubated for 2 hours at room

temperature or overnight at 4 °C in blocking solution (1:500): Cy5-conjugated donkey anti-rabbit (Jackson ImmunoResearch, #711-175-152) and Alexa Fluor 488–conjugated donkey anti-chicken (Jackson ImmunoResearch, #703-545-155). Images were acquired on a Leica SP8 confocal microscope at 1024 × 1024 resolution. Whole DRG were imaged in 60 mm glass-bottom dishes using 10× or 20× air objectives with 2–5 μm z-steps. Neuromas and contralateral nerves were captured by tile scan using a 10× air objective with 2 μm z-steps. Post-processing was performed with LAS X Life Science software (Leica).

Fiber density (fig. S8) was quantified from mCitrine reporter signal in neuromas and contralateral sciatic nerves using ImageJ. Each neuroma and contralateral nerve typically yielded ~20 and ~12 longitudinal cryosections, respectively; the middle three consecutive slices were selected to minimize epineurial interference. Images were converted to 8-bit grayscale, background-subtracted, and thresholded to generate binary masks of axonal fibers. A 50 × 50 μm region of interest (ROI) was placed at the neuroma tip or corresponding contralateral nerve center, and the axon-occupied area within this ROI was measured. Fiber density was expressed as the fraction of axon-positive area relative to total ROI area. Values from three slices were averaged to obtain one measurement per sample.

snRNA-seq of DRG across pain conditions

From a parent cohort of 60 mice, L4 and L5 DRG were collected from 18 mice (9 males and 9 females) that consistently exhibited a high-pain phenotype across 8–10 weeks post-SNT, with phenotyping performed weekly and tissue collected at 10 weeks, and from

18 mice (9 males and 9 females) that consistently exhibited a low-pain phenotype over the same period. 36 contralateral L4 and L5 DRG from both high- and low-pain mice were combined as the control group.

All nuclear extraction steps were performed on ice, or at 4 °C. Frozen L4 and L5 DRG, collected on dry ice in DNA/RNA LoBind tubes (Qiagen) were homogenized in NST buffer: 50 ml NST buffer contained 25 ml of 2x ST buffer, 1ml of 10% IGPAL, 1.4 ml of 35% BSA, and 22.6 ml nuclease-free water, and was prepared from ST buffer, containing 146 mM NaCl, 10 mM Tris-HCl, pH 7.5, 1 mM $CaCl_2$, and 21 mM $MgCl_2$ (*62*). For each sample, 7.5 ml of ST and 7.5 ml of NST buffer were prepared and 10 µl of RNasin was added to each. For each sample, 1 ml cold NST buffer (on ice) was added directly to the tube containing frozen DRG, allowed to thaw for 15–30 seconds, and DRG were transferred to a 7 ml Dounce Wheaton homogenizer containing 4 ml of NST buffer, and homogenized with 5 strokes with the loose pestle and 15 strokes with the tight pestle. The homogenate was then filtered through a 40 µm cell filter into a 50 ml Falcon tube on ice. 5 ml of ST buffer was added to the homogenizer, and any remaining homogenate was collected and also pipetted through the 40 µm cell filter. 10 ml of filtered homogenate then filtered through a 20 µm cell filter into a 15 ml Falcon tube on ice. The homogenizer was thoroughly rinsed between samples. Samples were centrifuged at 500 × g for 10 min at 4 °C. The supernatant was removed and the pellet was resuspended in 1 ml of ST buffer. 10 µl of Hoechst was added for a final conc. of 0.5 µg/ml, and the samples were FACS sorted to isolate nuclei.

Nuclei suspensions were sequenced using 10x Genomics assays, resuspended, and loaded into 10x Chromium device for snRNA-seq (10x Genomics 3’ v3). Libraries were

prepared for snRNA-seq according to the manufacturer's protocol. Libraries were sequenced on an Illumina NovaSeqX (Azenta). Sequencing data were processed and mapped to the mouse (mm10) genome using 10x Genomics cellranger v9 using default parameters. We ran the remove-background function of Cellbender (v0.3.0) to remove ambient RNA and empty droplets from raw expression matrices using default parameters.

We followed a similar cell type annotation and clustering approach as previous described (*25, 43*), and adopted the established physiological nomenclature for each neuronal subtype as shown in Table 1 in reference (*26*) and Fig. 1C in reference (*25*). Seurat v4 was used to perform quality control, data normalization, cell type annotation and comparison between neuroma conditions (*63*). Nuclei with >1000 genes and <10% of mitochondrial counts were included for analysis. We found 2000 variable genes for each library after log-normalization, and then integration anchors were selected across all libraries. The data were then scaled, and we selected PCs on the basis of the point where the PC only contributes to 5% of SD of highly variable gene expression and all PCs cumulatively contributed to 90% of the SD of highly variable gene expression. The libraries were then integrated using Seurat's CCA algorithm, and nuclei were clustered and plotted in UMAP space at a resolution of 0.5. A Wilcoxon rank sum test was performed between the clusters to identify marker genes. We annotated clusters that were *Snap25*$^{+}$ ($\log_2$FC > 0.5 and adjusted P value < 0.05 relative to all other clusters) as "neurons" and clusters that were *Sparc*$^{+}$ ($\log_2$FC > 0.5 and adjusted P value < 0.05 relative to all other clusters) as "non-neurons." Neurons were then separated and reintegrated using a resolution of 1. We annotated neurons using marker gene expression (fig. S6A; $\log_2$FC > 0.5; adjusted p-value < 0.05 relative to all other clusters). Clusters were labeled as

doublets if they contained both expression of *Snap25*, *Mpz*, and *Sparc* ($\log_2$FC > 0.5 and adjusted P value < 0.05 relative to all other clusters). Doublets were then removed, and the nuclei were reintegrated using the same parameters as described and then reannotated for a final time. To identify genes differentially expressed between conditions within each subtype, we used the Wilcoxon rank-sum test.

Directional concordance scores for each gene within each cell type were computed from its $\log_2$ fold-change ($\log_2$FC) values between the high-pain vs. low-pain and high-pain vs. control comparisons (fig. S6C), defined as:

$$\begin{cases} +\sqrt{|\log_2\mathrm{FC}_{\text{high pain/low pain}} \cdot \log_2\mathrm{FC}_{\text{high pain/control}}|}, \text{if both } \log_2\mathrm{FC} > 0 \text{ (upregulated in both)} \\ -\sqrt{|\log_2\mathrm{FC}_{\text{high pain/low pain}} \cdot \log_2\mathrm{FC}_{\text{high pain/control}}|}, \text{if both } \log_2\mathrm{FC} < 0 \text{ (downregulated in both)} \\ 0, \text{otherwise (opposite directions or no change)} \end{cases}$$

For gene ontology (GO) analysis, we used EnrichR (*64*) to assess functional enrichment. We selected genes significantly enriched in the SSTR2$^+$ population under the high pain condition ($\log_2$FC > 0.5; adjusted P < 0.05), compared to either the SSTR2$^+$ cells in the low-pain condition or the contralateral control condition. As the background gene list, we used all genes expressed in the SSTR2$^+$ population.

Statistical analysis

All statistical analyses, except for snRNA-seq data, were performed using GraphPad Prism, with the exact tests and *p* values reported in the figures, figure legends, or source data.

ACKNOWLEDGMENTS

We thank Dr. Bruce P. Bean and members of the Woolf and Ginty laboratories for their constructive feedback. We also thank the IDDRC Animal Behavior and Physiology Core, funded by NIH/NICHD P50HD105351 and IDDRC Cellular Imaging Core, funded by NIH P50 HD105351 at Boston Children's Hospital. Schematics and illustrations were created with BioRender.com. **Funding:** This work was supported by the International Human Frontier Science Program Organization LT0026/2023-L (X.Z.), NIH grants R35NS105076 (C.J.W.), R35NS097344 (D.D.G.), and R01AT011447 (D.D.G. and C.J.W.), the Edward R. and Anne G. Lefler Center for Neurodegenerative Disorders (D.D.G.), and the K. Lisa Yang Brain Body Center at Harvard Medical School (D.D.G.). D.D.G. is an investigator of the Howard Hughes Medical Institute. This article is subject to HHMI's Open Access to Publications policy. HHMI lab heads have previously granted a nonexclusive CC BY 4.0 license to the public and a sublicensable license to HHMI in their research articles. Pursuant to those licenses, the author-accepted manuscript of this article can be made freely available under a CC BY 4.0 license immediately upon publication. **Author contributions:** X.Z., D.D.G., and C.J.W. conceived the study. X.Z. performed all experiments and analyzed the data, with assistance from R.M.G. (optogenetics), S.A.B. (snRNA-seq), K.H. (histology), N.M.B., E.B., and E.S. (behavioral studies and histology), K.W. (LED cuff design), O.B. (automated behavioral screen), B.L.T. (acute pain experiments), S.S.J. and B.G.E. (tissue collection for snRNA-seq), M.Q.H. (home-cage EMG setup), C.S. (Piezo2-knockout experiments), K.L. and E.O.A. (generation of transgenic mouse lines), and I.F. (LED cuff calibration). A.R. provided expertise and oversight of the home-cage EMG experiments. B.R.J. provided expertise on and assisted

with the transcutaneous neuroma poke tests. B.J.W. provided expertise and oversight of the behavioral experiments. W.R. provided expertise and oversight of the snRNA-seq experiments. S.P.L. provided expertise and oversight of LED cuff design. D.D.G. and C.J.W. supervised the project. X.Z., D.D.G., and C.J.W. wrote the manuscript with input from all authors. **Competing interests:** C.J.W. is a founder of Nocion Therapeutics, Quralis, and BlackBox Bio. He also is a member of the scientific advisory boards of Lundbeck Pharma, Axonis, and Tafalgie Therapeutics. **Data and materials availability:** All data supporting the findings of this study are available within the article and its supplementary materials. Reagents are available from the corresponding author upon reasonable request.

References

1. D. Bouhassira *et al.*, Comparison of pain syndromes associated with nervous or somatic lesions and development of a new neuropathic pain diagnostic questionnaire (DN4). *Pain* **114**, 29-36 (2005).
2. D. Bouhassira *et al.*, Development and validation of the Neuropathic Pain Symptom Inventory. *Pain* **108**, 248-257 (2004).
3. C. Maier *et al.*, Quantitative sensory testing in the German Research Network on Neuropathic Pain (DFNS): somatosensory abnormalities in 1236 patients with different neuropathic pain syndromes. *Pain* **150**, 439-450 (2010).
4. J. Sandkuhler, Models and mechanisms of hyperalgesia and allodynia. *Physiol Rev* **89**, 707-758 (2009).
5. A. Tappe-Theodor, R. Kuner, Studying ongoing and spontaneous pain in rodents--challenges and opportunities. *Eur J Neurosci* **39**, 1881-1890 (2014).
6. D. J. Langford *et al.*, Coding of facial expressions of pain in the laboratory mouse. *Nat Methods* **7**, 447-449 (2010).
7. T. King *et al.*, Unmasking the tonic-aversive state in neuropathic pain. *Nat Neurosci* **12**, 1364-1366 (2009).
8. N. Attal *et al.*, Neuropathic pain: are there distinct subtypes depending on the aetiology or anatomical lesion? *Pain* **138**, 343-353 (2008).
9. Q. Zheng *et al.*, Synchronized cluster firing, a distinct form of sensory neuron activation, drives spontaneous pain. *Neuron* **110**, 209-220 e206 (2022).
10. L. Djouhri, S. Koutsikou, X. Fang, S. McMullan, S. N. Lawson, Spontaneous pain, both neuropathic and inflammatory, is related to frequency of spontaneous firing in intact C-fiber nociceptors. *J Neurosci* **26**, 1281-1292 (2006).
11. G. Wu *et al.*, Early onset of spontaneous activity in uninjured C-fiber nociceptors after injury to neighboring nerve fibers. *J Neurosci* **21**, RC140 (2001).
12. G. Wu *et al.*, Degeneration of myelinated efferent fibers induces spontaneous activity in uninjured C-fiber afferents. *J Neurosci* **22**, 7746-7753 (2002).
13. H. Kehlet, T. S. Jensen, C. J. Woolf, Persistent postsurgical pain: risk factors and prevention. *Lancet* **367**, 1618-1625 (2006).
14. C. D. Hwang *et al.*, Biology and pathophysiology of symptomatic neuromas. *Pain* **165**, 550-564 (2024).
15. N. S. Buch, E. Qerama, N. Brix Finnerup, L. Nikolajsen, Neuromas and postamputation pain. *Pain* **161**, 147-155 (2020).
16. R. B. Fillingim, Individual differences in pain: understanding the mosaic that makes pain personal. *Pain* **158 Suppl 1**, S11-S18 (2017).
17. O. Barkai *et al.*, A machine learning tool with light-based image analysis for automatic classification of 3D pain behaviors. *Cell Rep Methods*, 101145 (2025).
18. P. P. Su, L. He, L. Zhang, J. Yu, Z. Guan, Saphenous-sural nerve injury: a sensory-specific rodent model of neuropathic pain without motor deficits. *Pain*, (2025).
19. J. R. Bumgarner, W. H. Walker, 2nd, R. J. Nelson, Circadian rhythms and pain. *Neurosci Biobehav Rev* **129**, 296-306 (2021).

20. K. M. C. Oliveira *et al.*, Time course of traumatic neuroma development. *PLoS One* **13**, e0200548 (2018).
21. D. M. J. Arnold *et al.*, Diagnostic Criteria for Symptomatic Neuroma. *Ann Plast Surg* **82**, 420-427 (2019).
22. A. Miclescu, M. Schmelz, T. Gordh, Differential analgesic effects of subanesthetic concentrations of lidocaine on spontaneous and evoked pain in human painful neuroma: A randomized, double blind study. *Scand J Pain* **8**, 37-44 (2015).
23. I. Decosterd, C. J. Woolf, Spared nerve injury: an animal model of persistent peripheral neuropathic pain. *Pain* **87**, 149-158 (2000).
24. M. A. Nassar *et al.*, Nociceptor-specific gene deletion reveals a major role for Nav1.7 (PN1) in acute and inflammatory pain. *Proc Natl Acad Sci U S A* **101**, 12706-12711 (2004).
25. S. A. Bhuiyan *et al.*, Harmonized cross-species cell atlases of trigeminal and dorsal root ganglia. *Sci Adv* **10**, eadj9173 (2024).
26. L. Qi *et al.*, A mouse DRG genetic toolkit reveals morphological and physiological diversity of somatosensory neuron subtypes. *Cell* **187**, 1508-1526 e1516 (2024).
27. F. Michoud *et al.*, Epineural optogenetic activation of nociceptors initiates and amplifies inflammation. *Nat Biotechnol* **39**, 179-185 (2021).
28. A. H. Cooper *et al.*, Peripheral nerve injury results in a biased loss of sensory neuron subpopulations. *Pain* **165**, 2863-2876 (2024).
29. J. Turecek, D. D. Ginty, Coding of self and environment by Pacinian neurons in freely moving animals. *Neuron* **112**, 3267-3277 e3266 (2024).
30. D. A. Yarmolinsky *et al.*, Differential modification of ascending spinal outputs in acute and chronic pain states. *Neuron* **113**, 1223-1239 e1225 (2025).
31. N. S. Chowdhury *et al.*, Predicting Individual Pain Sensitivity Using a Novel Cortical Biomarker Signature. *JAMA Neurol* **82**, 237-246 (2025).
32. R. Dhandapani *et al.*, Control of mechanical pain hypersensitivity in mice through ligand-targeted photoablation of TrkB-positive sensory neurons. *Nat Commun* **9**, 1640 (2018).
33. S. E. Murthy *et al.*, The mechanosensitive ion channel Piezo2 mediates sensitivity to mechanical pain in mice. *Sci Transl Med* **10**, (2018).
34. X. Zeng, R. Powell, C. J. Woolf, Mechanism-based nonopioid analgesic targets. *J Clin Invest* **135**, (2025).
35. C. E. Morris, P. F. Juranka, Nav channel mechanosensitivity: activation and inactivation accelerate reversibly with stretch. *Biophys J* **93**, 822-833 (2007).
36. T. Kretschmer *et al.*, Ankyrin G and voltage gated sodium channels colocalize in human neuroma--key proteins of membrane remodeling after axonal injury. *Neurosci Lett* **323**, 151-155 (2002).
37. J. A. Black, L. Nikolajsen, K. Kroner, T. S. Jensen, S. G. Waxman, Multiple sodium channel isoforms and mitogen-activated protein kinases are present in painful human neuromas. *Ann Neurol* **64**, 644-653 (2008).
38. V. Madigan, F. Zhang, J. E. Dahlman, Drug delivery systems for CRISPR-based genome editors. *Nat Rev Drug Discov* **22**, 875-894 (2023).

39. A. Raj, A. van Oudenaarden, Nature, nurture, or chance: stochastic gene expression and its consequences. *Cell* **135**, 216-226 (2008).
40. Z. Ren, Y. Tan, L. Zhao, Cell Heterogeneity and Variability in Peripheral Nerve after Injury. *Int J Mol Sci* **25**, (2024).
41. R. C. Cannon, C. O'Donnell, M. F. Nolan, Stochastic ion channel gating in dendritic neurons: morphology dependence and probabilistic synaptic activation of dendritic spikes. *PLoS Comput Biol* **6**, (2010).
42. L. Znaor, S. Lovric, Q. Hogan, D. Sapunar, Association of neural inflammation with hyperalgesia following spinal nerve ligation. *Croat Med J* **48**, 35-42 (2007).
43. W. Renthal *et al.*, Transcriptional Reprogramming of Distinct Peripheral Sensory Neuron Subtypes after Axonal Injury. *Neuron* **108**, 128-144 e129 (2020).
44. H. Yan, W. Gao, Z. Pan, F. Zhang, C. Fan, The expression of alpha-SMA in the painful traumatic neuroma: potential role in the pathobiology of neuropathic pain. *J Neurotrauma* **29**, 2791-2797 (2012).
45. S. Deininger *et al.*, Nerve injury converts Schwann cells in a long-term repair-like state in human neuroma tissue. *Exp Neurol* **382**, 114981 (2024).
46. W. Weng *et al.*, Significance of alpha smooth muscle actin expression in traumatic painful neuromas: a pilot study in rats. *Sci Rep* **6**, 23828 (2016).
47. J. Khan, N. Noboru, A. Young, D. Thomas, Pro and anti-inflammatory cytokine levels (TNF-alpha, IL-1beta, IL-6 and IL-10) in rat model of neuroma. *Pathophysiology* **24**, 155-159 (2017).
48. P. J. Austin *et al.*, Evidence for a distinct neuro-immune signature in rats that develop behavioural disability after nerve injury. *J Neuroinflammation* **12**, 96 (2015).
49. C. Alexandre *et al.*, Nociceptor spontaneous activity is responsible for fragmenting non-rapid eye movement sleep in mouse models of neuropathic pain. *Sci Transl Med* **16**, eadg3036 (2024).
50. C. Alexandre *et al.*, Decreased alertness due to sleep loss increases pain sensitivity in mice. *Nat Med* **23**, 768-774 (2017).
51. Z. Zhang *et al.*, Automated preclinical detection of mechanical pain hypersensitivity and analgesia. *Pain* **163**, 2326-2336 (2022).
52. S. R. Chaplan, F. W. Bach, J. W. Pogrel, J. M. Chung, T. L. Yaksh, Quantitative assessment of tactile allodynia in the rat paw. *J Neurosci Methods* **53**, 55-63 (1994).
53. C. Santiago *et al.*, Activity-dependent development of the body's touch receptors. *Neuron* **113**, 1758-1773 e1759 (2025).
54. K. Nonomura *et al.*, Piezo2 senses airway stretch and mediates lung inflation-induced apnoea. *Nature* **541**, 176-181 (2017).
55. A. Giovannucci *et al.*, CaImAn an open source tool for scalable calcium imaging data analysis. *Elife* **8**, (2019).
56. W. Olson *et al.*, Sparse genetic tracing reveals regionally specific functional organization of mammalian nociceptors. *Elife* **6**, (2017).
57. V. E. Abraira *et al.*, The Cellular and Synaptic Architecture of the Mechanosensory Dorsal Horn. *Cell* **168**, 295-310 e219 (2017).
58. M. Rutlin *et al.*, The cellular and molecular basis of direction selectivity of Adelta-LTMRs. *Cell* **159**, 1640-1651 (2014).

59. L. Han *et al.*, A subpopulation of nociceptors specifically linked to itch. *Nat Neurosci* **16**, 174-182 (2013).
60. S. Vrontou, A. M. Wong, K. K. Rau, H. R. Koerber, D. J. Anderson, Genetic identification of C fibres that detect massage-like stroking of hairy skin in vivo. *Nature* **493**, 669-673 (2013).
61. S. Choi *et al.*, Parallel ascending spinal pathways for affective touch and pain. *Nature* **587**, 258-263 (2020).
62. M. Slyper *et al.*, A single-cell and single-nucleus RNA-Seq toolbox for fresh and frozen human tumors. *Nat Med* **26**, 792-802 (2020).
63. Y. Hao *et al.*, Integrated analysis of multimodal single-cell data. *Cell* **184**, 3573-3587 e3529 (2021).
64. E. Y. Chen *et al.*, Enrichr: interactive and collaborative HTML5 gene list enrichment analysis tool. *BMC Bioinformatics* **14**, 128 (2013).
65. D. J. Burek *et al.*, Inflammatory pain in mice induces light cycle-dependent effects on sleep architecture. *Neuropsychopharmacology* **50**, 1595-1605 (2025).

Fig.1

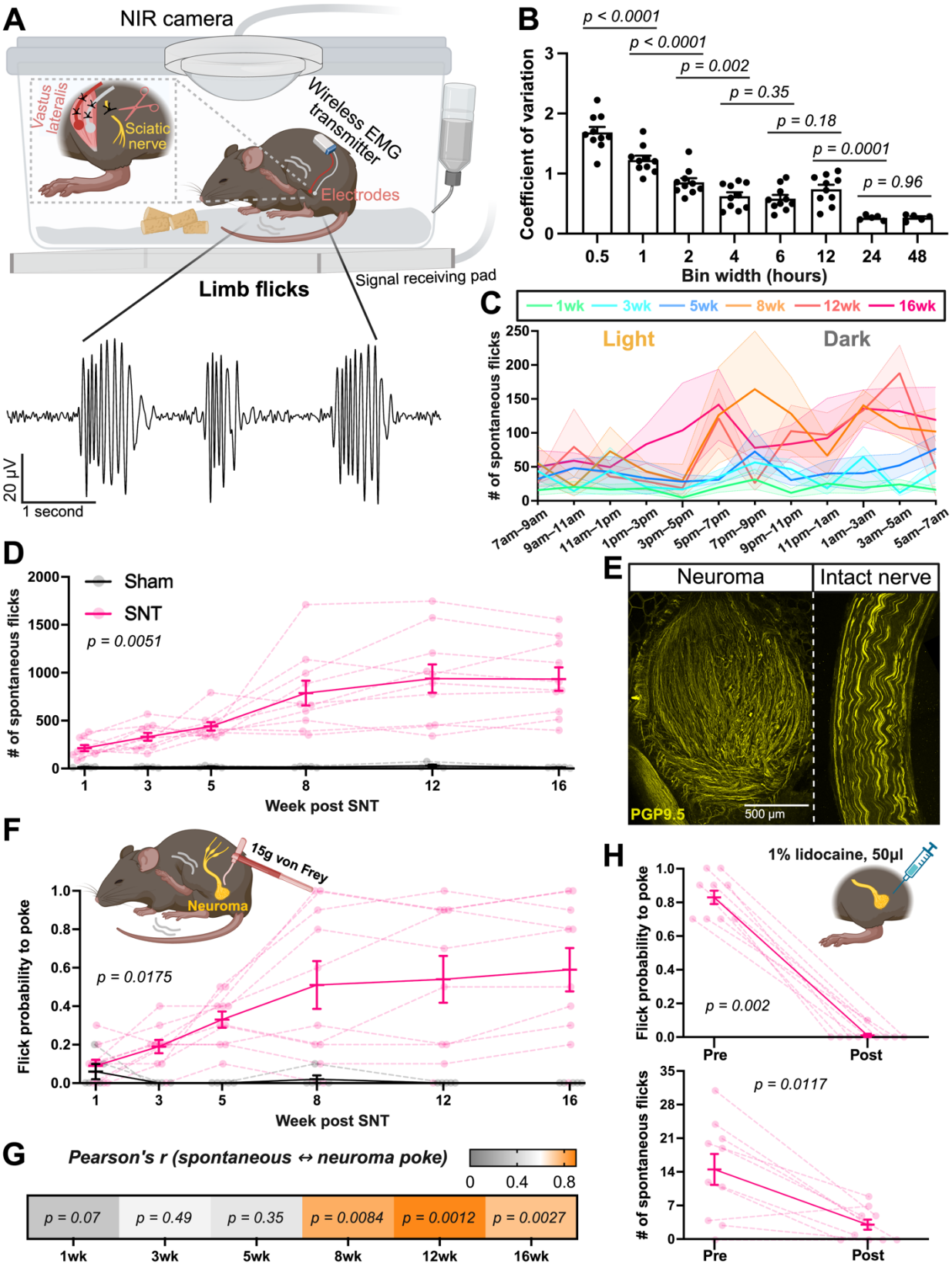
A
NIR camera
Vastus lateralis
Sciatic nerve
Wireless EMG transmitter
Electrodes
Signal receiving pad
Limb flicks
20 µV
1 second
B
p < 0.0001
p < 0.0001
p = 0.002
p = 0.35
p = 0.18
p = 0.0001
p = 0.96
Coefficient of variation
Bin width (hours)
0.5
1
2
4
6
12
24
48
C
1wk
3wk
5wk
8wk
12wk
16wk
Light
Dark
# of spontaneous flicks
7am–9am
9am–11am
11am–1pm
1pm–3pm
3pm–5pm
5pm–7pm
7pm–9pm
9pm–11pm
11pm–1am
1am–3am
3am–5am
5am–7am
D
Sham
SNT
p = 0.0051
# of spontaneous flicks
Week post SNT
E
Neuroma
Intact nerve
PGP9.5
500 µm
F
15g von Frey
Neuroma
p = 0.0175
Flick probability to poke
Week post SNT
G
Pearson's r (spontaneous ↔ neuroma poke)
0
0.4
0.8
p = 0.07
p = 0.49
p = 0.35
p = 0.0084
p = 0.0012
p = 0.0027
1wk
3wk
5wk
8wk
12wk
16wk
H
1% lidocaine, 50µl
Flick probability to poke
p = 0.002
Pre
Post
# of spontaneous flicks
p = 0.0117
Pre
Post

Fig. 1. Neuromas drive chronic spontaneous neuropathic pain. (**A**) Schematic of the home-cage EMG/video recording system (top) and representative EMG trace of limb flick bouts (bottom) after a sciatic nerve transection (SNT). (**B**) Coefficient of variation of spontaneous limb flick counts when a 24-hour recording was binned at different intervals (0.5, 1, 2, 4, 6, 12 hours). Each dot represents one mouse (n = 10 mice, 8 weeks post-SNT). A subset of 5 mice was recorded for 6 consecutive days to calculate 24- and 48-hour variation. P values from two-sided paired t-tests except for 12 vs 24 hours (unpaired t-test). (**C**) Spontaneous limb flick counts quantified in 2-hour bins over 24 hours at indicated time points post-SNT. Light phase: 7:00 a.m.–7:00 p.m.; dark phase: 7:00 p.m.–7:00 a.m. Solid lines and shaded bands represent mean ± SEM across n = 10 mice. (**D**) Total 24-hour spontaneous flick counts in individual mice after sham surgery (n = 5) or SNT (n = 10). Data are mean ± SEM; dashed lines connect individual mice. P values from two-way ANOVA with Tukey's multiple comparisons (figure shows the interaction effect of sham vs SNT over time; see source data for full statistical results). (**E**) Confocal images of a neuroma (8 weeks post-SNT) and contralateral intact nerve labeled with a neuronal axonal marker PGP9.5. (**F**) Flick probability in response to transcutaneous neuroma poke after sham surgery or SNT in the same mice shown in (D). (**G**) Pearson’s correlation between spontaneous flick counts (D) and flick probability (F) at indicated time points post-SNT. (**H**) Flick probability to poke (top) and spontaneous flick counts over 30 minutes (bottom) before and after local lidocaine injection at the neuroma site (8–12 weeks post-SNT, n = 10 mice). Data are mean ± SEM; dashed lines connect individual mice. P values from two-sided Wilcoxon matched-pairs signed-rank test.

Fig.2

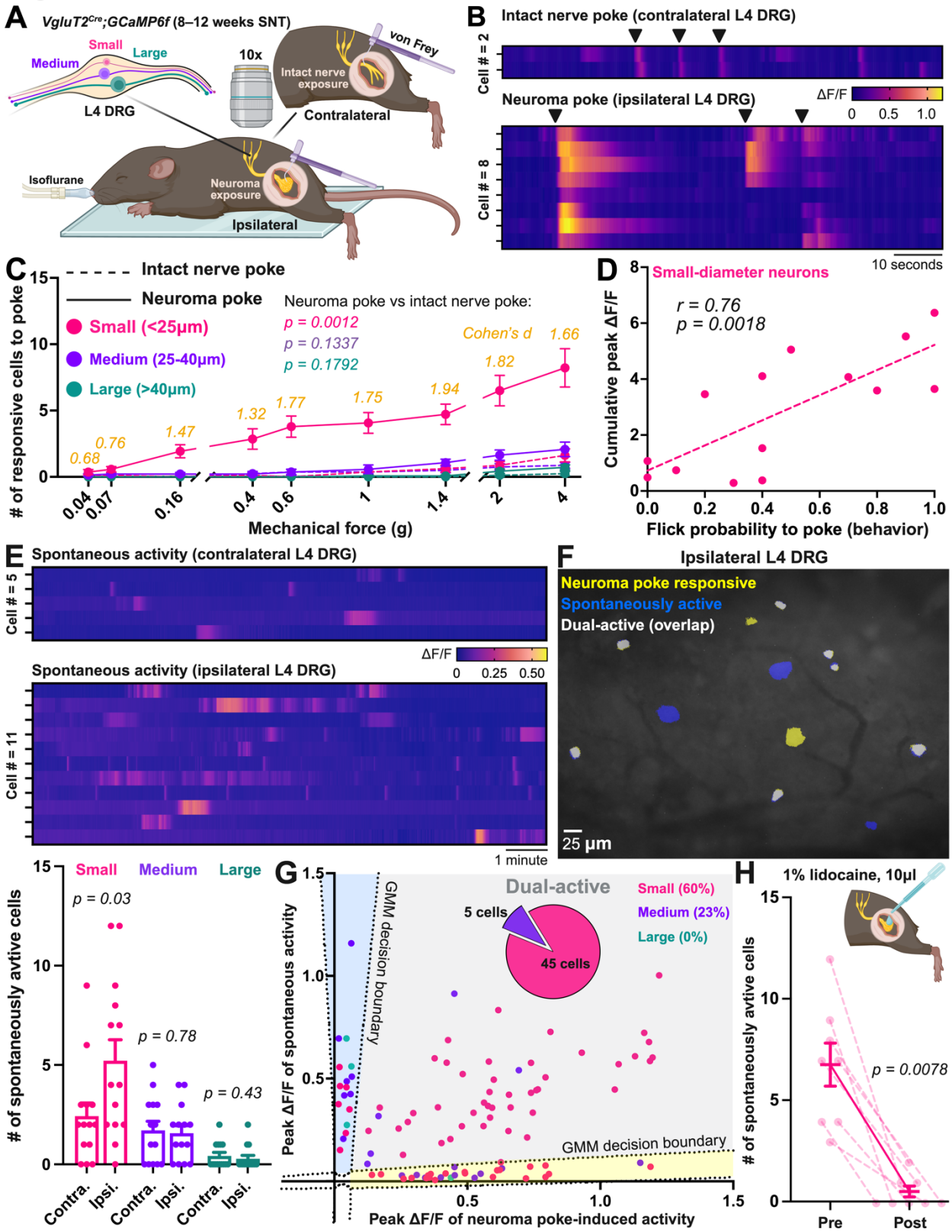
A
VgluT2Cre;GCaMP6f (8–12 weeks SNT)
Small
Large
Medium
L4 DRG
10x
Intact nerve exposure
von Frey
Contralateral
Isoflurane
Neuroma exposure
Ipsilateral
B
Intact nerve poke (contralateral L4 DRG)
Cell # = 2
Neuroma poke (ipsilateral L4 DRG)
ΔF/F
0
0.5
1.0
Cell # = 8
10 seconds
C
Intact nerve poke
Neuroma poke
Small (<25μm)
Medium (25-40μm)
Large (>40μm)
Neuroma poke vs intact nerve poke:
p = 0.0012
p = 0.1337
p = 0.1792
Cohen's d
0.68
0.76
1.47
1.32
1.77
1.75
1.94
1.82
1.66
# of responsive cells to poke
Mechanical force (g)
D
Small-diameter neurons
r = 0.76
p = 0.0018
Cumulative peak ΔF/F
Flick probability to poke (behavior)
E
Spontaneous activity (contralateral L4 DRG)
Cell # = 5
ΔF/F
0
0.25
0.50
Spontaneous activity (ipsilateral L4 DRG)
Cell # = 11
1 minute
F
Ipsilateral L4 DRG
Neuroma poke responsive
Spontaneously active
Dual-active (overlap)
25 μm
Small
Medium
Large
p = 0.03
p = 0.78
p = 0.43
# of spontaneously avtive cells
Contra.
Ipsi.
G
Dual-active
5 cells
45 cells
Small (60%)
Medium (23%)
Large (0%)
GMM decision boundary
Peak ΔF/F of spontaneous activity
Peak ΔF/F of neuroma poke-induced activity
H
1% lidocaine, 10μl
p = 0.0078
# of spontaneously avtive cells
Pre
Post

Fig. 2. Small-diameter DRG neurons respond to neuroma poke and exhibit ectopic spontaneous activity. (**A**) Schematic of the *in vivo* DRG imaging setup. (**B**) Representative calcium activity heatmaps from individual DRG neurons in response to a neuroma poke or contralateral intact nerve poke. Arrowheads indicate stimulus timing. (**C**) Quantification of responsive cells by soma diameter, small (<25 μm), medium (25–40 μm), and large (>40 μm), across a range of mechanical forces applied with von Frey filaments. Data are mean ± SEM from 14 ipsilateral and contralateral L4 DRGs (n = 14 mice). P values from two-way ANOVA with Tukey's multiple comparisons (shown for the interaction effect of neuroma poke vs intact nerve poke across mechanical forces; see source data for full statistical results). Cohen's d effect sizes are shown for small-diameter neurons (neuroma poke vs. intact nerve poke). (**D**) Pearson's correlation between the cumulative peak ΔF/F of responsive small-diameter DRG neurons to neuroma poke (1.4 g von Frey) and behavioral flick probability to transcutaneous neuroma poke. Each dot represents one mouse. (**E**) Representative heatmaps of spontaneous calcium activity from individual neurons in contralateral and ipsilateral L4 DRG (top), and quantification of spontaneously active cells of each size during 30-minute recordings (bottom). Data are mean ± SEM; each dot represents one L4 DRG (n = 14 mice). P values from two-sided paired t-test. (**F**) Example overlay of cells spontaneously active (blue) and cells responsive to neuroma poke (yellow); dual-active cells are white. (**G**) Classification of cells solely responsive to neuroma poke, solely spontaneously active, or dual-active, based on peak activity amplitude determined by Gaussian Mixture Model (GMM) boundaries (dashed lines). Percentages indicate the proportion of dual-active cells relative to the total number of cells of each size. Pie chart depicts the cell distribution within the dual-active category. Each dot represents one cell. Red, small-diameter; purple, medium-diameter; green, large-diameter DRG neurons. (**H**) Number of spontaneously active small-diameter cells before and 5 minutes after topical application of lidocaine to the neuroma. Data are mean ± SEM; dashed lines connect ipsilateral L4 DRG from individual mice (n = 8). P value from two-sided Wilcoxon matched-pairs signed-rank test.

Fig.3

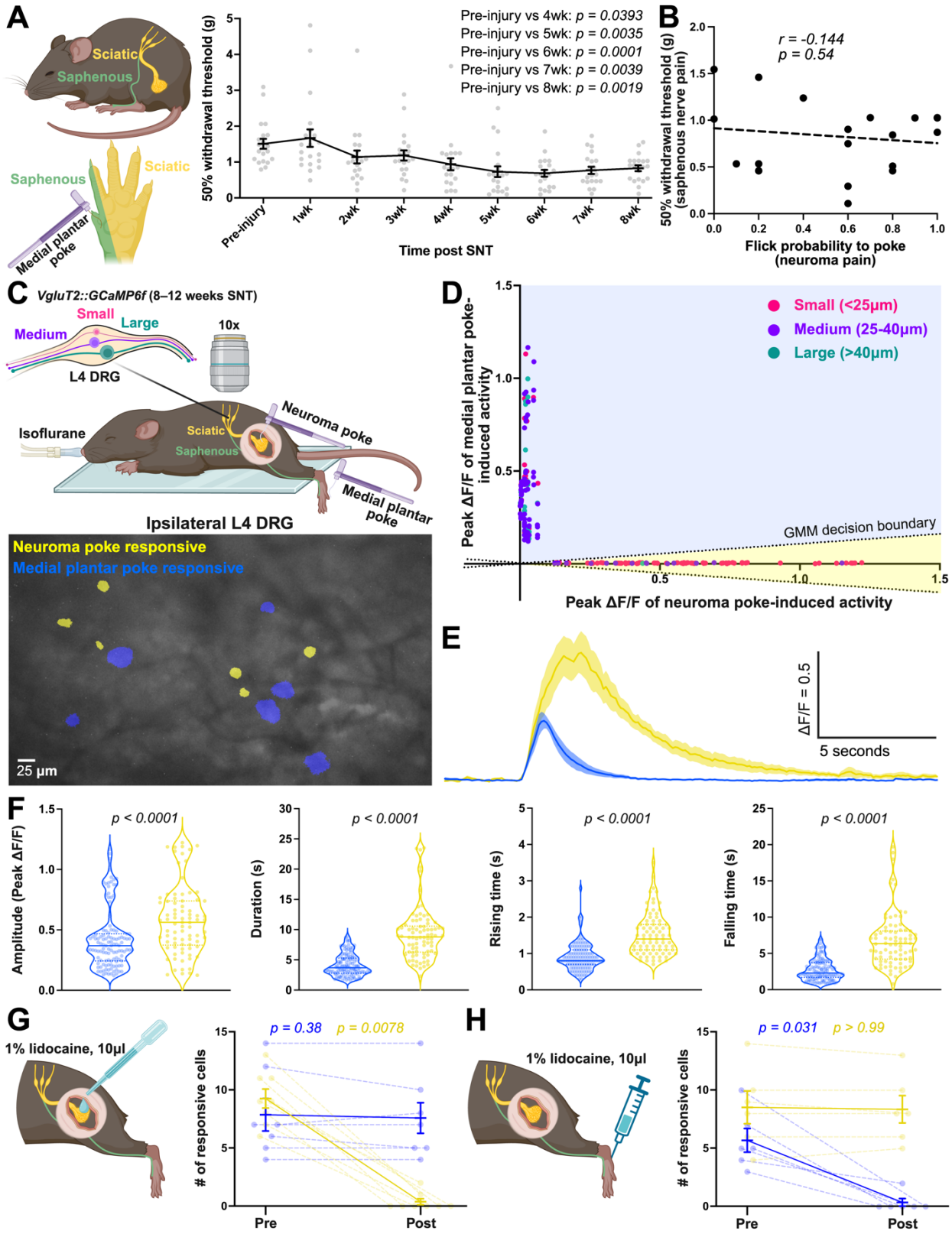
A
Sciatic
Saphenous
Saphenous
Sciatic
Medial plantar poke
50% withdrawal threshold (g)
Pre-injury vs 4wk: p = 0.0393
Pre-injury vs 5wk: p = 0.0035
Pre-injury vs 6wk: p = 0.0001
Pre-injury vs 7wk: p = 0.0039
Pre-injury vs 8wk: p = 0.0019
Pre-injury
1wk
2wk
3wk
4wk
5wk
6wk
7wk
8wk
Time post SNT
B
r = -0.144
p = 0.54
50% withdrawal threshold (g) (saphenous nerve pain)
Flick probability to poke (neuroma pain)
C
VgluT2::GCaMP6f (8–12 weeks SNT)
Small
Large
Medium
L4 DRG
10x
Isoflurane
Sciatic
Saphenous
Neuroma poke
Medial plantar poke
Ipsilateral L4 DRG
Neuroma poke responsive
Medial plantar poke responsive
25 µm
D
Small (<25µm)
Medium (25-40µm)
Large (>40µm)
Peak ΔF/F of medial plantar poke-induced activity
GMM decision boundary
Peak ΔF/F of neuroma poke-induced activity
E
ΔF/F = 0.5
5 seconds
F
Amplitude (Peak ΔF/F)
p < 0.0001
Duration (s)
p < 0.0001
Rising time (s)
p < 0.0001
Falling time (s)
p < 0.0001
G
1% lidocaine, 10µl
# of responsive cells
p = 0.38
p = 0.0078
Pre
Post
H
1% lidocaine, 10µl
# of responsive cells
p = 0.031
p > 0.99
Pre
Post

Fig. 3. Distinct DRG neuron populations mediate pain from intact versus injured fibers. (**A**) Schematic of the plantar von Frey assay targeting the medial plantar area innervated by the intact saphenous nerve (left) and quantification of the 50% withdrawal threshold (right). Each dot represents one mouse (n = 20). Data are mean ± SEM. P values from one-way ANOVA with Tukey's multiple-comparisons test. (**B**) Pearson's correlation between the 50% withdrawal threshold from medial plantar poke and flick probability to transcutaneous neuroma poke at 8 weeks post-SNT. Each dot represents one mouse. (**C**) Schematic of the *in vivo* L4 DRG calcium imaging setup for neuroma or medial plantar poke with a 1.4 g von Frey filament (top), and an example overlay showing cells responsive to neuroma poke and medial plantar poke (bottom). (**D**) Classification of cells responsive to neuroma poke or medial plantar poke based on peak ΔF/F amplitude determined by GMM boundaries (dashed lines). Each dot represents one cell; no dual-responsive cells were observed. (**E**) Calcium traces from neuroma poke–responsive (yellow) and medial plantar poke–responsive (blue) cells. Shaded bands indicate mean ± SEM from n = 5 mice (neuroma) and n = 4 mice (medial plantar). (**F**) Quantification of response amplitude, duration, rising time, and falling time for each group. Each dot represents one cell. P values from two-sided Mann–Whitney tests. (**G**, **H**) Number of cells responsive to a neuroma poke (yellow) or a medial plantar poke (blue) before and after topical lidocaine application to the neuroma (G) or intraplantar injection (H). Tests were performed 5 minutes after lidocaine administration. Data are mean ± SEM; dashed lines connect individual mice (n = 8 for neuroma application, n = 6 for medial plantar injection). P values from two-sided Wilcoxon matched-pairs signed-rank tests.

Fig.4

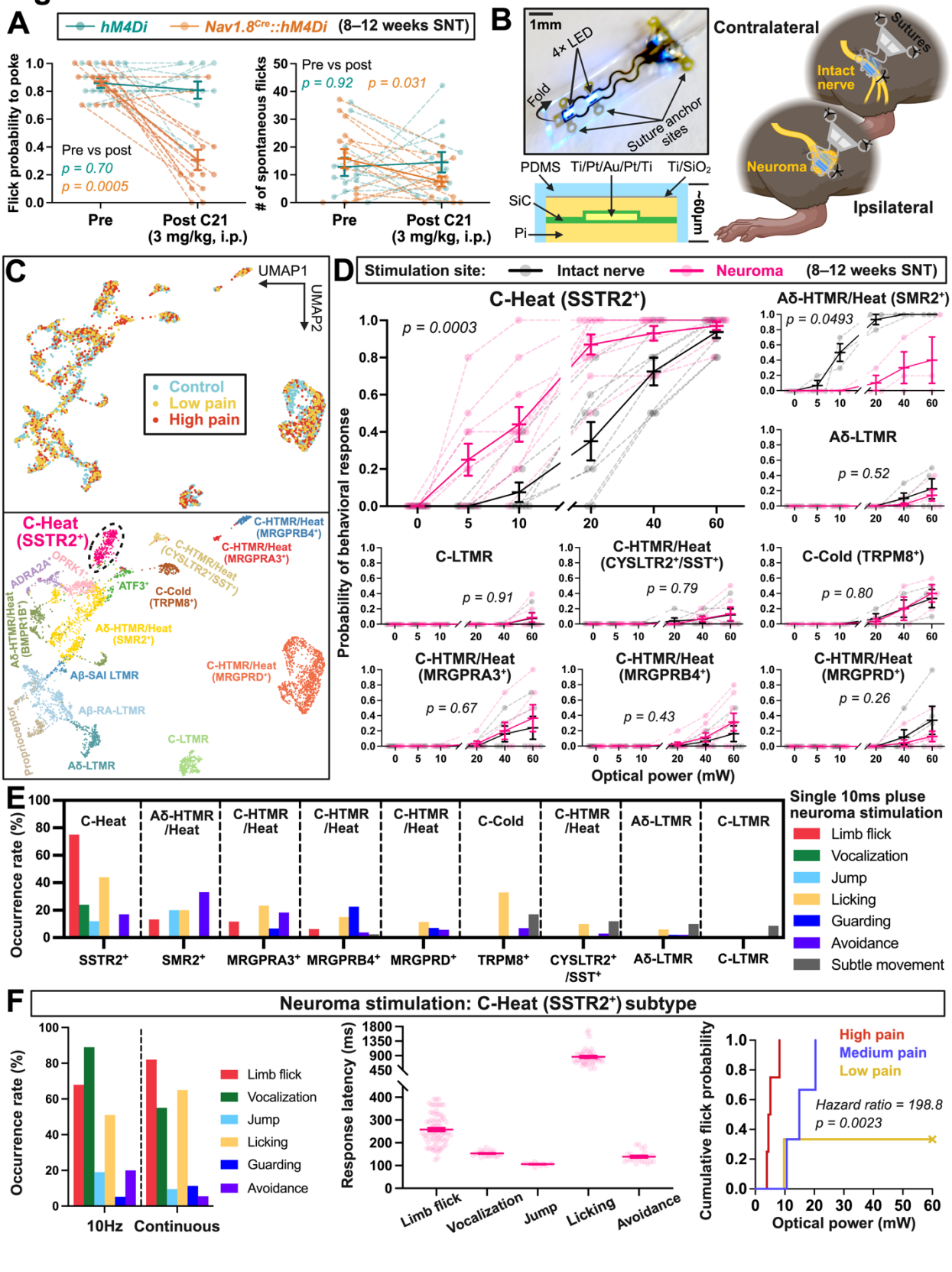
A
hM4Di
Nav1.8Cre::hM4Di
(8–12 weeks SNT)
Flick probability to poke
Pre vs post
p = 0.70
p = 0.0005
Pre
Post C21
(3 mg/kg, i.p.)
# of spontaneous flicks
Pre vs post
p = 0.92
p = 0.031
B
1mm
4× LED
Fold
Suture anchor sites
PDMS
Ti/Pt/Au/Pt/Ti
Ti/SiO2
SiC
Pi
~60μm
Contralateral
Sutures
Intact nerve
Neuroma
Ipsilateral
C
UMAP1
UMAP2
Control
Low pain
High pain
C-Heat (SSTR2+)
C-HTMR/Heat (MRGPRB4+)
C-HTMR/Heat (MRGPRA3+)
C-HTMR/Heat (CYSLTR2+/SST+)
ATF3+
C-Cold (TRPM8+)
Aδ-HTMR/Heat (SMR2+)
Aβ-SAI LTMR
C-HTMR/Heat (MRGPRD+)
Aβ-RA-LTMR
C-LTMR
Aδ-LTMR
Proprioceptor
D
Stimulation site:
Intact nerve
Neuroma
(8–12 weeks SNT)
C-Heat (SSTR2+)
p = 0.0003
Aδ-HTMR/Heat (SMR2+)
p = 0.0493
Aδ-LTMR
p = 0.52
C-LTMR
p = 0.91
C-HTMR/Heat (CYSLTR2+/SST+)
p = 0.79
C-Cold (TRPM8+)
p = 0.80
C-HTMR/Heat (MRGPRA3+)
p = 0.67
C-HTMR/Heat (MRGPRB4+)
p = 0.43
C-HTMR/Heat (MRGPRD+)
p = 0.26
Probability of behavioral response
Optical power (mW)
E
Occurrence rate (%)
C-Heat
Aδ-HTMR /Heat
C-HTMR /Heat
C-Cold
Aδ-LTMR
C-LTMR
SSTR2+
SMR2+
MRGPRA3+
MRGPRB4+
MRGPRD+
TRPM8+
CYSLTR2+ /SST+
Single 10ms pluse neuroma stimulation
Limb flick
Vocalization
Jump
Licking
Guarding
Avoidance
Subtle movement
F
Neuroma stimulation: C-Heat (SSTR2+) subtype
Occurrence rate (%)
10Hz
Continuous
Limb flick
Vocalization
Jump
Licking
Guarding
Avoidance
Response latency (ms)
Cumulative flick probability
High pain
Medium pain
Low pain
Hazard ratio = 198.8
p = 0.0023
Optical power (mW)

Fig. 4. SSTR2$^+$ sensory neurons drive limb flicks. (**A**) Flick probability to transcutaneous neuroma poke (left) and spontaneous flick counts over 30 minutes (right) before and after intraperitoneal injection (i.p.) of C21 in Nav1.8::hM4Di (n = 14) mice and hM4Di littermate controls (n = 12). Data are mean ± SEM; dashed lines connect individual mice. P values from two-sided Wilcoxon matched-pairs signed-rank test. (**B**) Photograph of the miniaturized blue LED cuff (top), schematic cross-section of the interconnects showing layered materials (bottom left; softness and flexibility were achieved by miniaturizing metal interconnects and incorporating soft polymer layers; see fig. S8 for details), and illustration of the implantation site for neuroma or intact sciatic nerve stimulation (right). (**C**) UMAP projections of DRG snRNA-seq showing nuclei from contralateral DRG (control), ipsilateral DRG from low-pain, and high-pain mice (top) and annotated sensory-neuron subtype identities (bottom). 10 weeks post-SNT mice were used for snRNA-seq. (**D**) Optogenetic activation of genetically defined neuronal subtypes (see Materials and Methods for the transgenic lines targeting each subtype). Optical power versus response probability for individual transgenic lines (10 trials per animal; single 10 ms pulse). Data are mean ± SEM; dashed lines connect individual mice. P values from two-way ANOVA with Tukey's multiple comparisons (shown for the interaction effect of neuroma vs intact nerve stimulation across optical powers; see source data for full statistical results and sample sizes). (**E**) Histograms showing the occurrence of different behaviors evoked at maximum optical neuroma stimulation (60 mW). Note that multiple behaviors could occur in a single trial. (**F**) Left: occurrence of behaviors in response to 5-s stimulation, delivered either as a 10 Hz train of 10-ms pulses or as continuous light. Middle: response latencies of individual behaviors relative to stimulus onset; data are mean ± SEM, each dot represents a single trial across n = 10 mice. Right: Cumulative flick probability (1 − Kaplan-Meier estimate) as a function of optical power for high-, medium-, and low-pain mice determined by transcutaneous neuroma poke. Cross mark at 60 mW indicates right-censoring for animals who did not show a flick at the maximum optical power.

Fig. S1

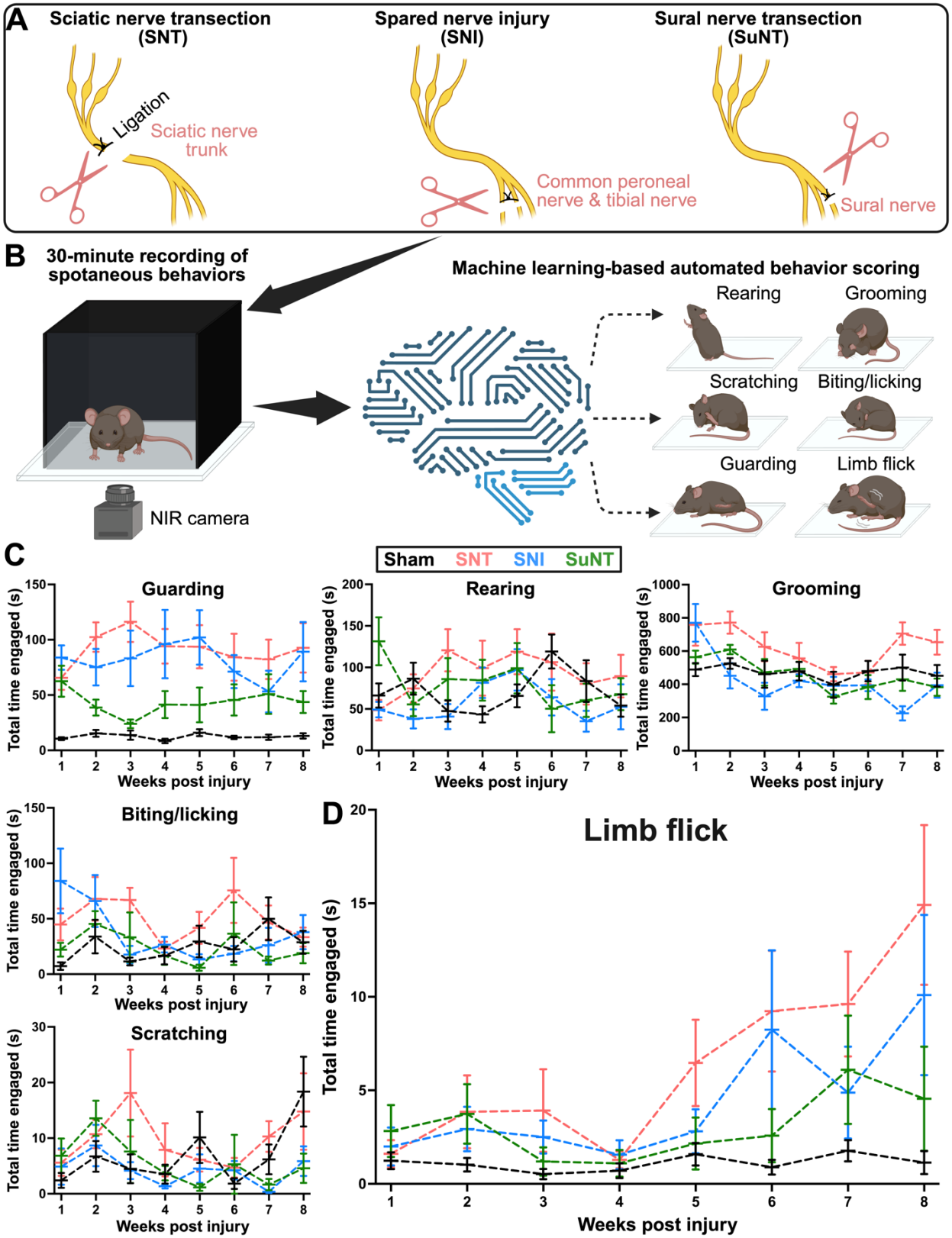
A
Sciatic nerve transection (SNT)
Ligation
Sciatic nerve trunk
Spared nerve injury (SNI)
Common peroneal nerve & tibial nerve
Sural nerve transection (SuNT)
Sural nerve
B
30-minute recording of spotaneous behaviors
NIR camera
Machine learning-based automated behavior scoring
Rearing
Grooming
Scratching
Biting/licking
Guarding
Limb flick
C
Sham
SNT
SNI
SuNT
Guarding
Rearing
Grooming
Biting/licking
Scratching
Total time engaged (s)
Weeks post injury
D
Limb flick

Fig. S1. Automated behavioral screening reveals limb flick as a prominent behavior in the chronic phase after peripheral nerve injury. (**A**) Schematics of four sciatic nerve injury models: sciatic nerve transection (SNT), spared nerve injury (SNI), and sural nerve transection (SuNT). (**B**) Experimental setup for 30-min recordings of spontaneous behaviors using a bottom-up near-infrared (NIR) camera and machine-learning–based automated scoring (*17*). (**C** and **D**) Total time spent on each indicated behavior on the injured side, measured weekly for up to 8 weeks post-injury. Lines represent group means, error bars indicate ± SEM. For each injury type, n = 8 mice (4 males, 4 females). Statistical analyses provided in the source data.

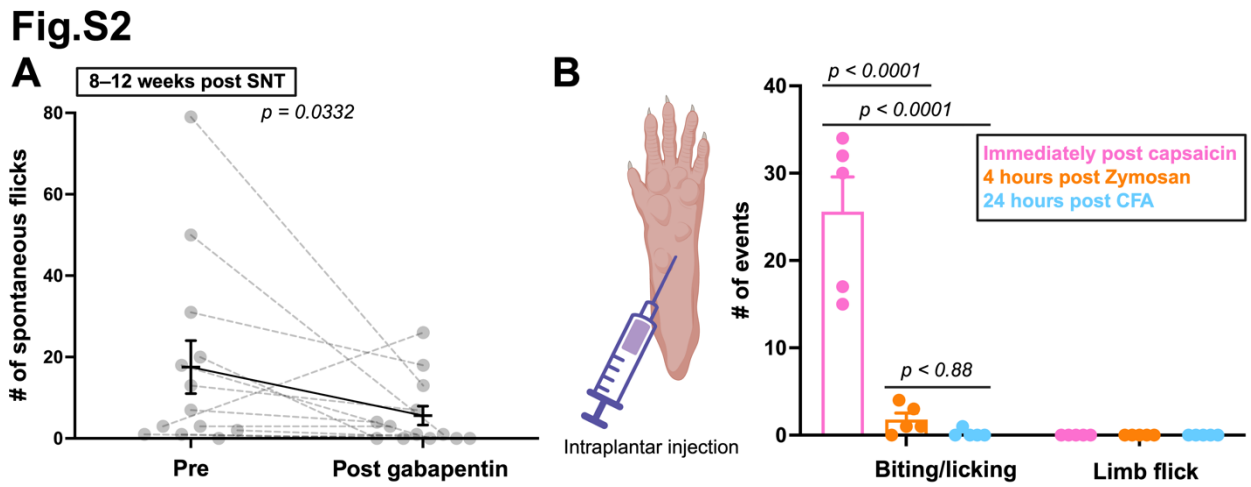

Fig. S2. Limb flicks are suppressed by gabapentin and are absent in acute pain conditions. (**A**) Spontaneous limb flicks quantified over 30 min before and after intraperitoneal gabapentin (30 mg/kg) at 8–12 weeks post-SNT (n = 13 mice). Data are mean ± SEM; dashed lines connect individual mice. P value from two-sided Wilcoxon matched-pairs signed-rank test. (**B**) Schematic of intraplantar injection (left) and quantification of biting/licking events and spontaneous limb flicks (right) following capsaicin (0.01%, 10 μL), Zymosan (100 μg in 10 μL), or CFA (100%, 10 μL) injection. Behaviors were recorded for 30 minutes at peak-response windows defined from literature: immediately after capsaicin (*17*), 4 hours after Zymosan (*51*), and 24 hours after CFA (*65*). Limb flicks are absent across all acute pain models, while biting and licking of the affected paw is the predominant behavior in the capsaicin model. Each dot represents one mouse (n = 5 per model). Data are mean ± SEM; P values from one-way ANOVA with Tukey's multiple-comparisons test.

Fig.S3

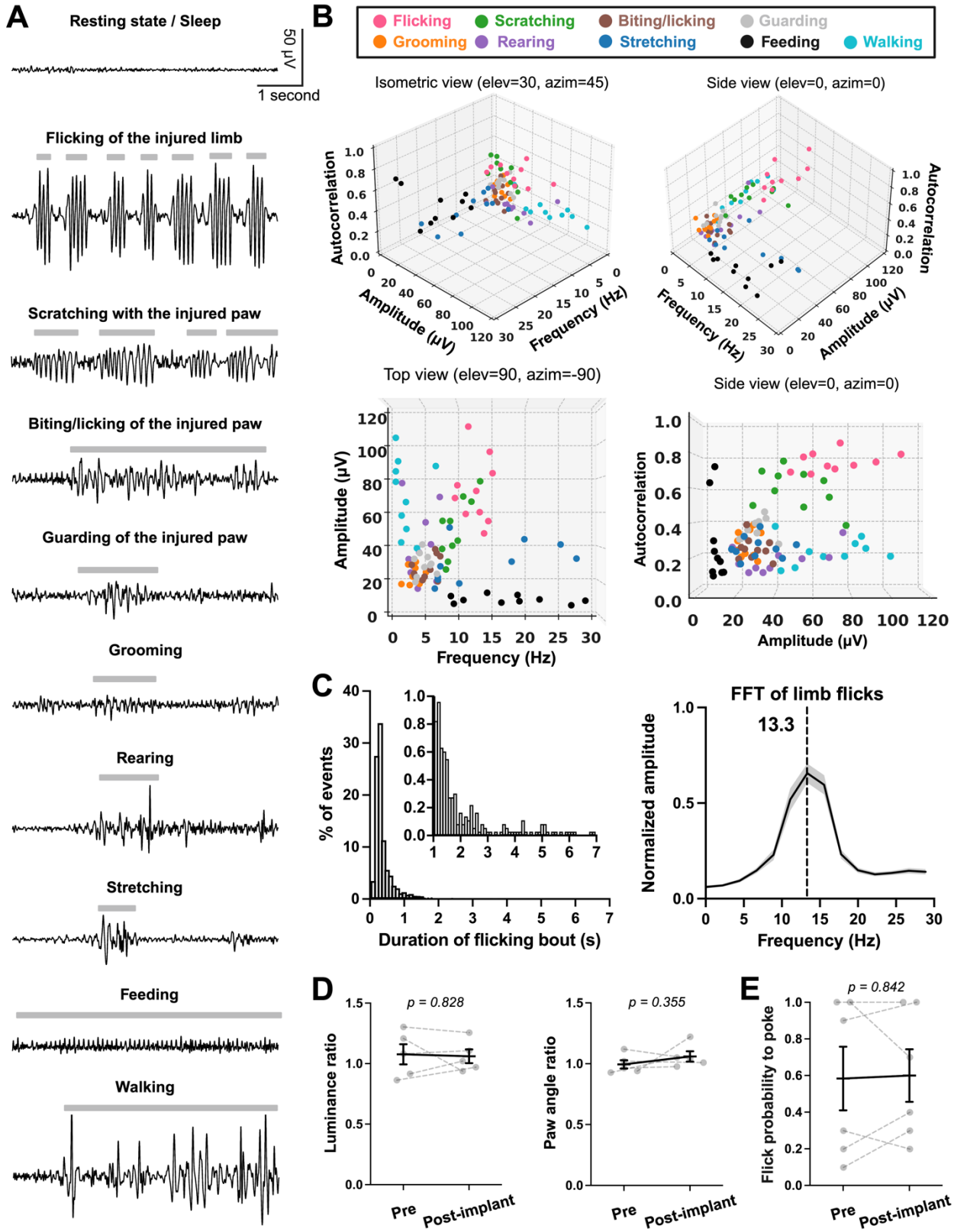
A
Resting state / Sleep
50 µV
1 second
Flicking of the injured limb
Scratching with the injured paw
Biting/licking of the injured paw
Guarding of the injured paw
Grooming
Rearing
Stretching
Feeding
Walking
B
Flicking
Scratching
Biting/licking
Guarding
Grooming
Rearing
Stretching
Feeding
Walking
Isometric view (elev=30, azim=45)
Side view (elev=0, azim=0)
Autocorrelation
Amplitude (µV)
Frequency (Hz)
Top view (elev=90, azim=-90)
Side view (elev=0, azim=0)
Amplitude (µV)
Frequency (Hz)
Autocorrelation
Amplitude (µV)
C
% of events
Duration of flicking bout (s)
FFT of limb flicks
13.3
Normalized amplitude
Frequency (Hz)
D
p = 0.828
Luminance ratio
Pre
Post-implant
p = 0.355
Paw angle ratio
Pre
Post-implant
E
p = 0.842
Flick probability to poke
Pre
Post-implant

Fig. S3. 24-hour EMG-based home-cage monitoring captures spontaneous limb flicks. (**A**) Representative EMG traces during various home-cage behaviors. Gray bars indicate periods when the behaviors occurred as confirmed by corresponding videos. (**B**) Feature plots of peak amplitude, frequency, and autocorrelation coefficient (first non-zero positive peak) of EMG trace for each behavior. Periodic movements such as limb flicks showed higher autocorrelation values. Each dot represents the average of 20 events from one mouse (n = 10 mice, 12 weeks post-SNT). Elev, elevation; azim, azimuth. (**C**) Left: histogram showing the duration distribution of individual limb flick bouts, with an inset expanding the 0–1% vs 1–7 seconds range. Most events occurred within 1 s. Right: Fast Fourier Transform (FFT) of limb flicks showing a dominant frequency at 13.3 Hz. (**D**) Weight bearing and gait parameters measured by luminance ratio (left) and paw angle ratio (right) (*51*) before and two weeks after implantation of the wireless telemetry device without nerve injury (n = 5 mice). (**E**) Flick probability to poke before and two weeks after implantation of the wireless EMG device (n = 6 mice at 8–10 weeks post-SNT). Data are mean ± SEM; dashed lines connect individual mice. P values from two-sided Wilcoxon matched-pairs signed-rank test in (D) and (E).

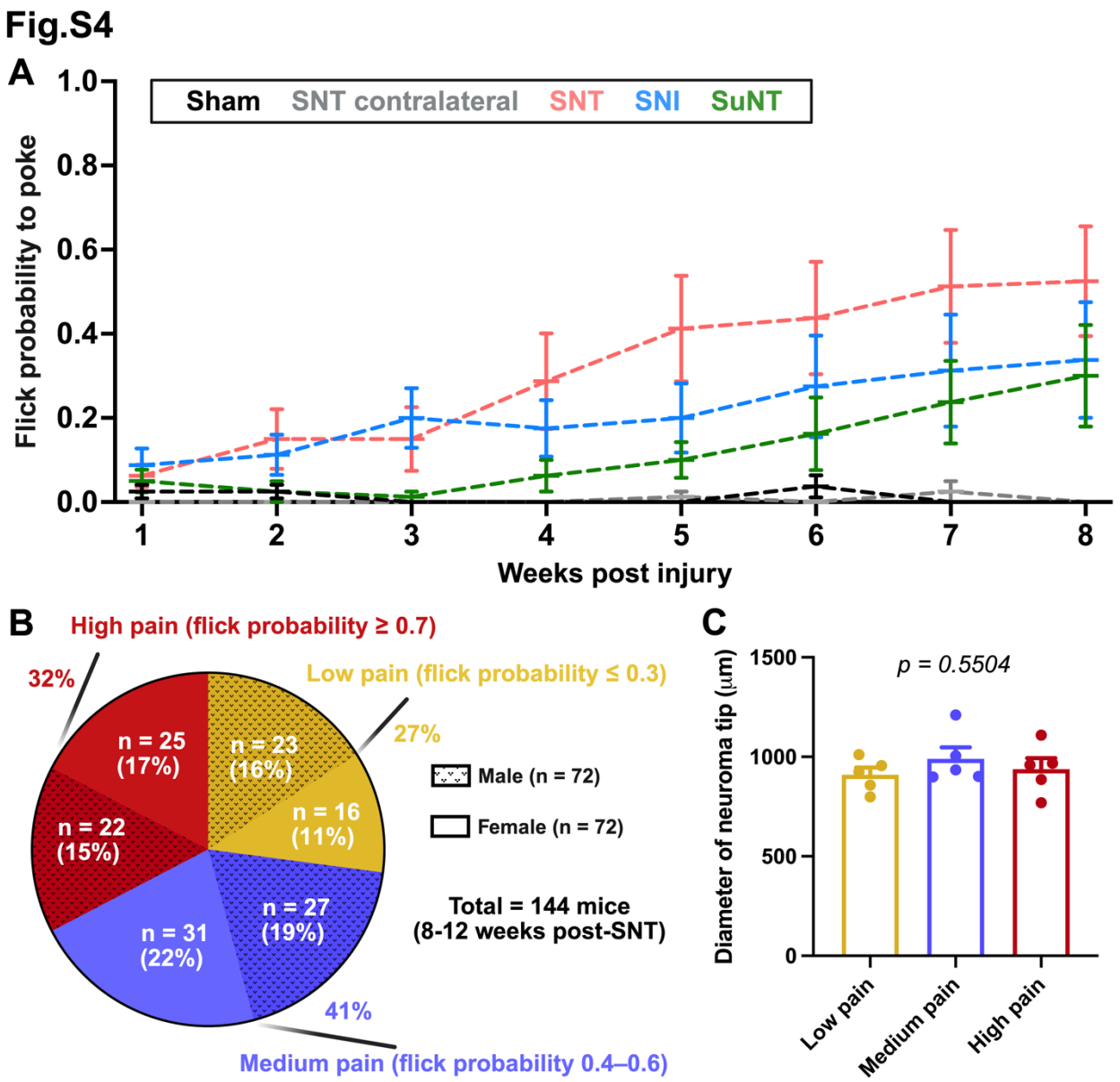

Fig. S4. Neuroma pain emerges across peripheral nerve injury models and shows differential pain severity. (**A**) Flick probability in response to transcutaneous neuroma poke measured weekly for up to 8 weeks after injury. Lines represent group means; error bars indicate ± SEM. For each injury type, n = 8 mice (4 males and 4 females, as in Fig. S1). Statistical analyses are provided in the source data. (**B**) Pie chart showing the distribution of high-pain, low-pain, and medium-pain phenotypes. (**C**) Histogram showing the size of neuromas in each pain condition. Each dot represents a neuroma (n = 5 mice for each condition). P value from one-way ANOVA.

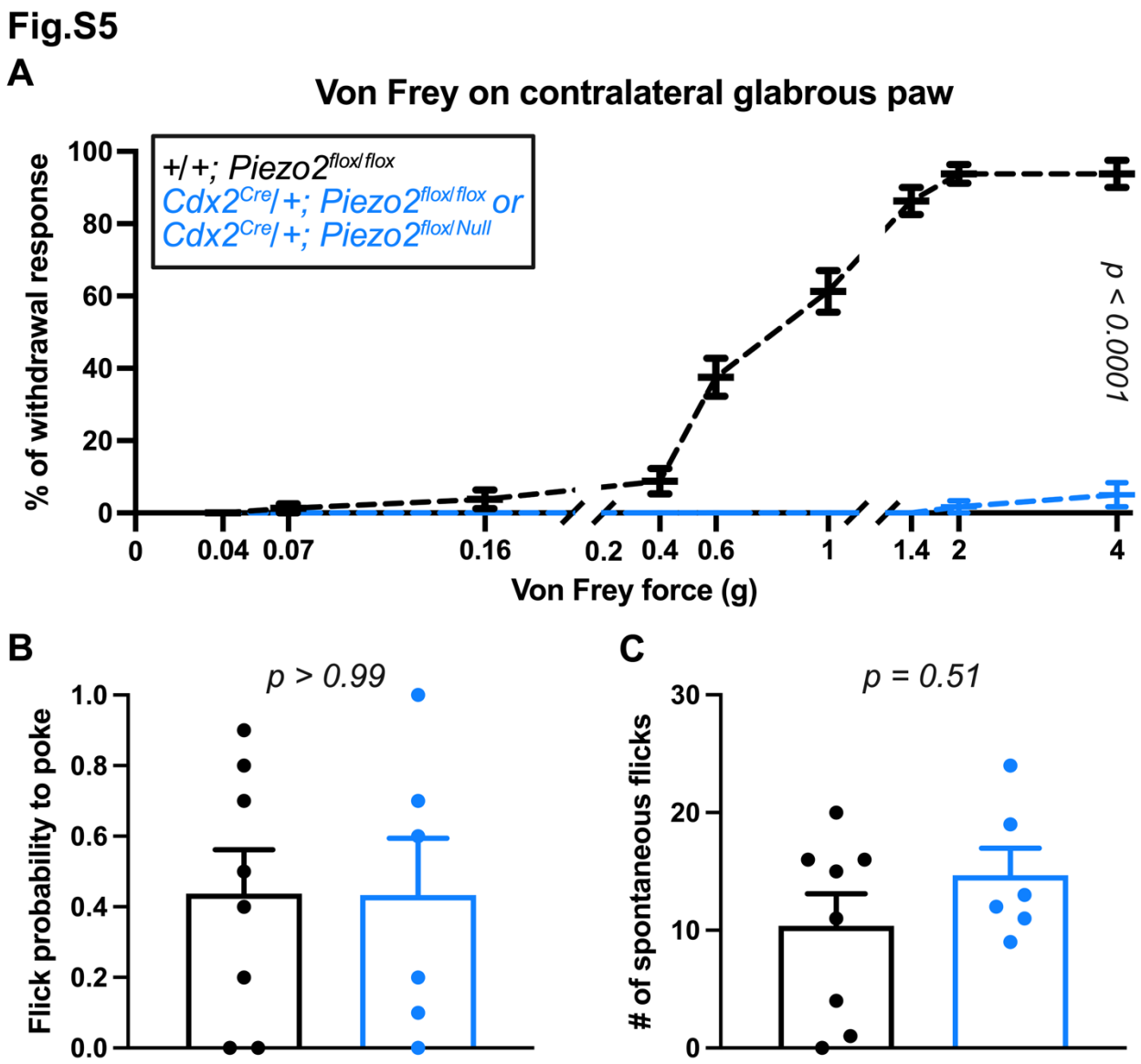

Fig. S5. Spontaneous limb flicks and flicks evoked by transcutaneous poke are independent of Piezo2. (**A**–**C**) Von Frey filament evoked responses from contralateral glabrous paw (A), flick probability to transcutaneous neuroma poke (B), and spontaneous flick count over 30 minutes (C) at 8 weeks post-SNT in control and Piezo2 conditional knockout mediated by *Cdx2*^{Cre} (*53*). Data are mean ± SEM; each dot represents one mouse (n = 8 controls, 6 knockouts). P values in (A) from two-way ANOVA with Tukey's multiple comparisons (figure shows the interaction effect of control vs knockout across von Frey forces; see source data for full statistical results), and from two-sided Mann–Whitney tests in (B) and (C).

Fig.S6

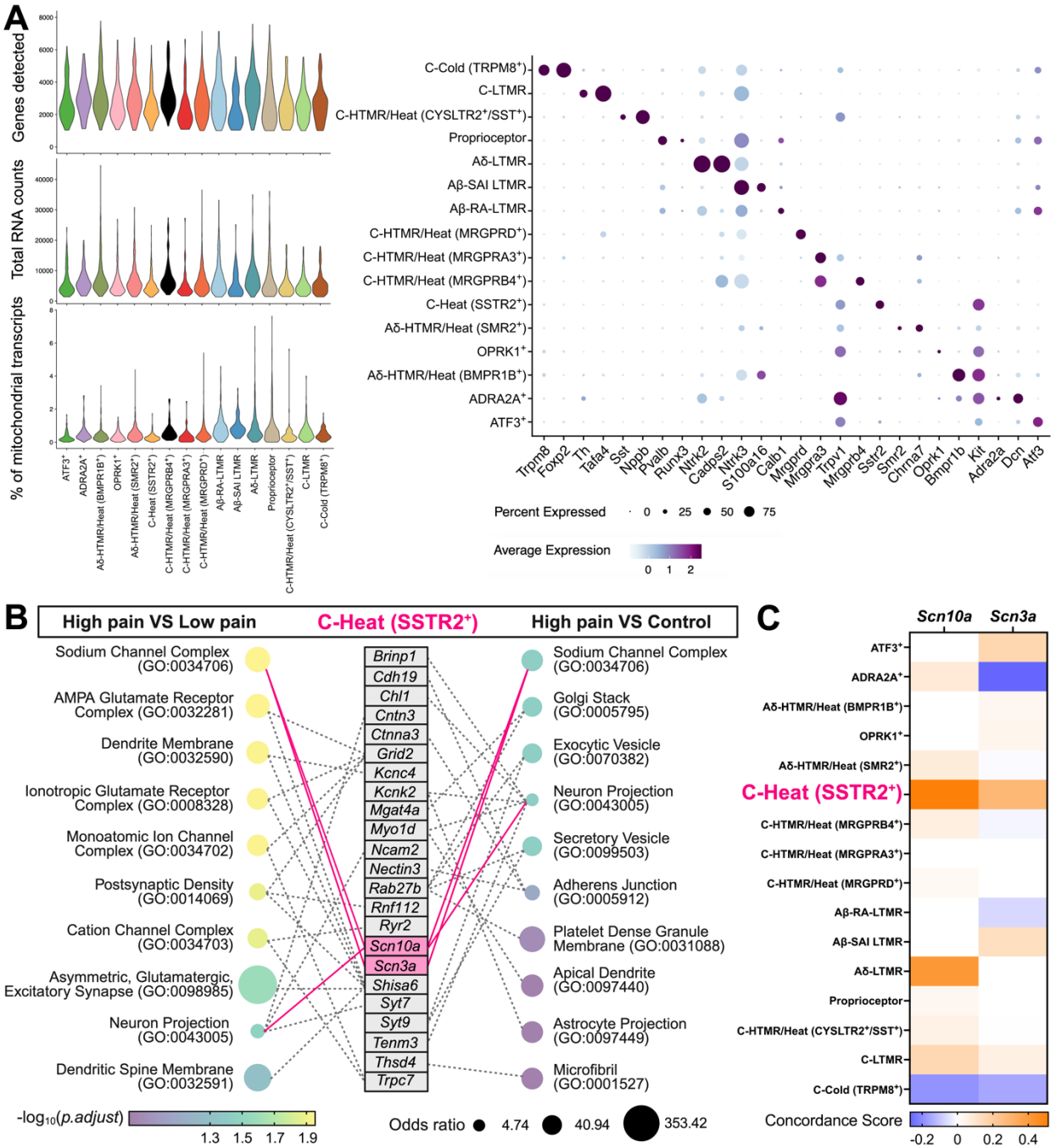
A
Genes detected
Total RNA counts
% of mitochondrial transcripts
ATF3+
ADRA2A+
Aδ-HTMR/Heat (BMPR1B+)
OPRK1+
Aδ-HTMR/Heat (SMR2+)
C-Heat (SSTR2+)
C-HTMR/Heat (MRGPRB4+)
C-HTMR/Heat (MRGPRA3+)
C-HTMR/Heat (MRGPRD+)
Aβ-RA-LTMR
Aβ-SAI LTMR
Aδ-LTMR
Proprioceptor
C-HTMR/Heat (CYSLTR2+/SST+)
C-LTMR
C-Cold (TRPM8+)
Trpm8
Foxp2
Th
Tafa4
Sst
Nppb
Pvalb
Runx3
Ntrk2
Cadps2
Ntrk3
S100a16
Calb1
Mrgprd
Mrgpra3
Trpv1
Mrgprb4
Sstr2
Smr2
Chrna7
Oprk1
Bmpr1b
Kit
Adra2a
Dcn
Atf3
Percent Expressed
0
25
50
75
Average Expression
0
1
2
B
High pain VS Low pain
C-Heat (SSTR2+)
High pain VS Control
Sodium Channel Complex (GO:0034706)
AMPA Glutamate Receptor Complex (GO:0032281)
Dendrite Membrane (GO:0032590)
Ionotropic Glutamate Receptor Complex (GO:0008328)
Monoatomic Ion Channel Complex (GO:0034702)
Postsynaptic Density (GO:0014069)
Cation Channel Complex (GO:0034703)
Asymmetric, Glutamatergic, Excitatory Synapse (GO:0098985)
Neuron Projection (GO:0043005)
Dendritic Spine Membrane (GO:0032591)
Brinp1
Cdh19
Chl1
Cntn3
Ctnna3
Grid2
Kcnc4
Kcnk2
Mgat4a
Myo1d
Ncam2
Nectin3
Rab27b
Rnf112
Ryr2
Scn10a
Scn3a
Shisa6
Syt7
Syt9
Tenm3
Thsd4
Trpc7
Sodium Channel Complex (GO:0034706)
Golgi Stack (GO:0005795)
Exocytic Vesicle (GO:0070382)
Neuron Projection (GO:0043005)
Secretory Vesicle (GO:0099503)
Adherens Junction (GO:0005912)
Platelet Dense Granule Membrane (GO:0031088)
Apical Dendrite (GO:0097440)
Astrocyte Projection (GO:0097449)
Microfibril (GO:0001527)
-log10(p.adjust)
1.3
1.5
1.7
1.9
Odds ratio
4.74
40.94
353.42
C
Scn10a
Scn3a
ATF3+
ADRA2A+
Aδ-HTMR/Heat (BMPR1B+)
OPRK1+
Aδ-HTMR/Heat (SMR2+)
C-Heat (SSTR2+)
C-HTMR/Heat (MRGPRB4+)
C-HTMR/Heat (MRGPRA3+)
C-HTMR/Heat (MRGPRD+)
Aβ-RA-LTMR
Aβ-SAI LTMR
Aδ-LTMR
Proprioceptor
C-HTMR/Heat (CYSLTR2+/SST+)
C-LTMR
C-Cold (TRPM8+)
Concordance Score
-0.2
0
0.2
0.4

Fig. S6. Transcriptomic profiling of DRG across pain conditions. (**A**) Violin plots showing quality control metrics, including the number of genes detected per nucleus (nFeature cutoff = 1,000), total RNA counts, and percentage of mitochondrial transcripts, and dot plots showing expression of canonical marker genes across neuronal populations. Dot size represents the percentage of nuclei expressing the gene, and dot color reflects average expression level. Cell-type annotations follow previously described criteria (*25, 43*). (**B**) Gene Ontology enrichment within the SSTR2^{+} population. Left: top 10 Cellular Component terms for high-pain vs. low-pain; right: top 10 Cellular Component terms for high-pain vs. control, ranked by adjusted P values. Middle column lists DEGs contributing to each term; solid magenta lines connect genes shared between contrasts, gray dashed lines connect genes appearing in only one contrast. (**C**) Concordance scores for *Scn10a* and *Scn3a* across sensory neuron subtypes. The score is positive when a gene is up-regulated in both comparisons (high-pain vs. low-pain and high-pain vs. control), negative when down-regulated in both, and zero when regulation is inconsistent or observed in only one comparison; larger magnitude indicates stronger concordance (see Materials and Methods for formula).

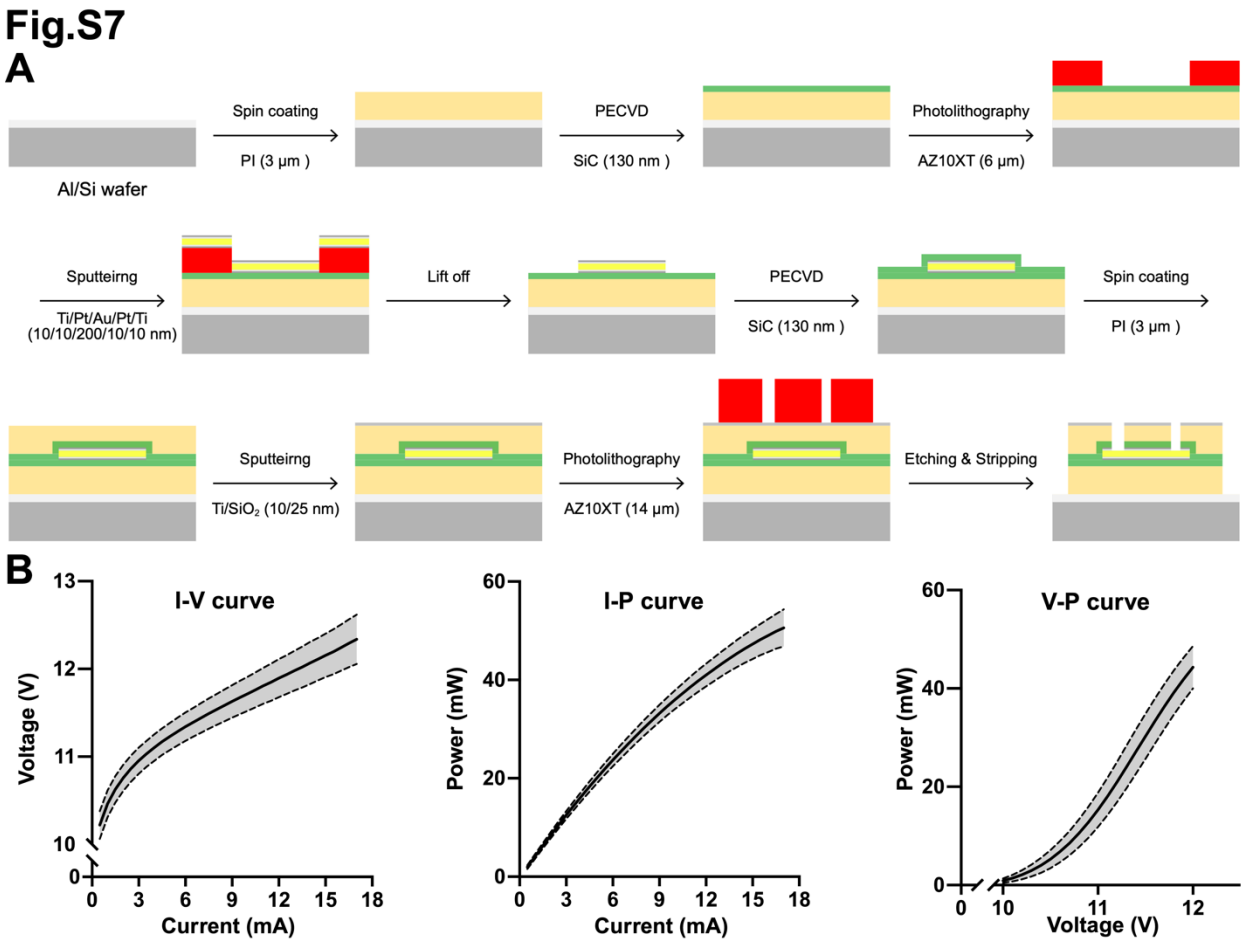

Fig. S7. Fabrication and characterization of the miniaturized LED cuff. (**A**) Schematic of the fabrication process. A 3-μm polyimide (PI) layer is spin-coated onto an aluminum (Al)/silicon (Si) wafer, serving as a sacrificial substrate, and baked to complete imidization. A 130-nm silicon carbide (SiC) layer is deposited by plasma-enhanced chemical vapor deposition (PECVD). Metal interconnects consisting of Titanium/Platinum/Gold/Platinum/Titanium (Ti/Pt/Au/Pt/Ti) (10/10/200/10/10 nm) are sputtered and patterned by lift-off, followed by deposition of a second SiC layer and an additional PI layer. A Ti/SiO_2 bilayer (10/25 nm) is sputtered on the surface, and final device patterning is performed by inductively coupled plasma–reactive ion etching (ICP-RIE) to define cuff geometry and electrode windows. (**B**) Electrical and optical performance of the integrated blue micro-LEDs (470 nm). Representative current–voltage (I–V), current–power (I–P), and voltage–power (V–P) curves. Solid lines and shaded bands represent mean ± SEM across n = 24 devices.

Fig.S8

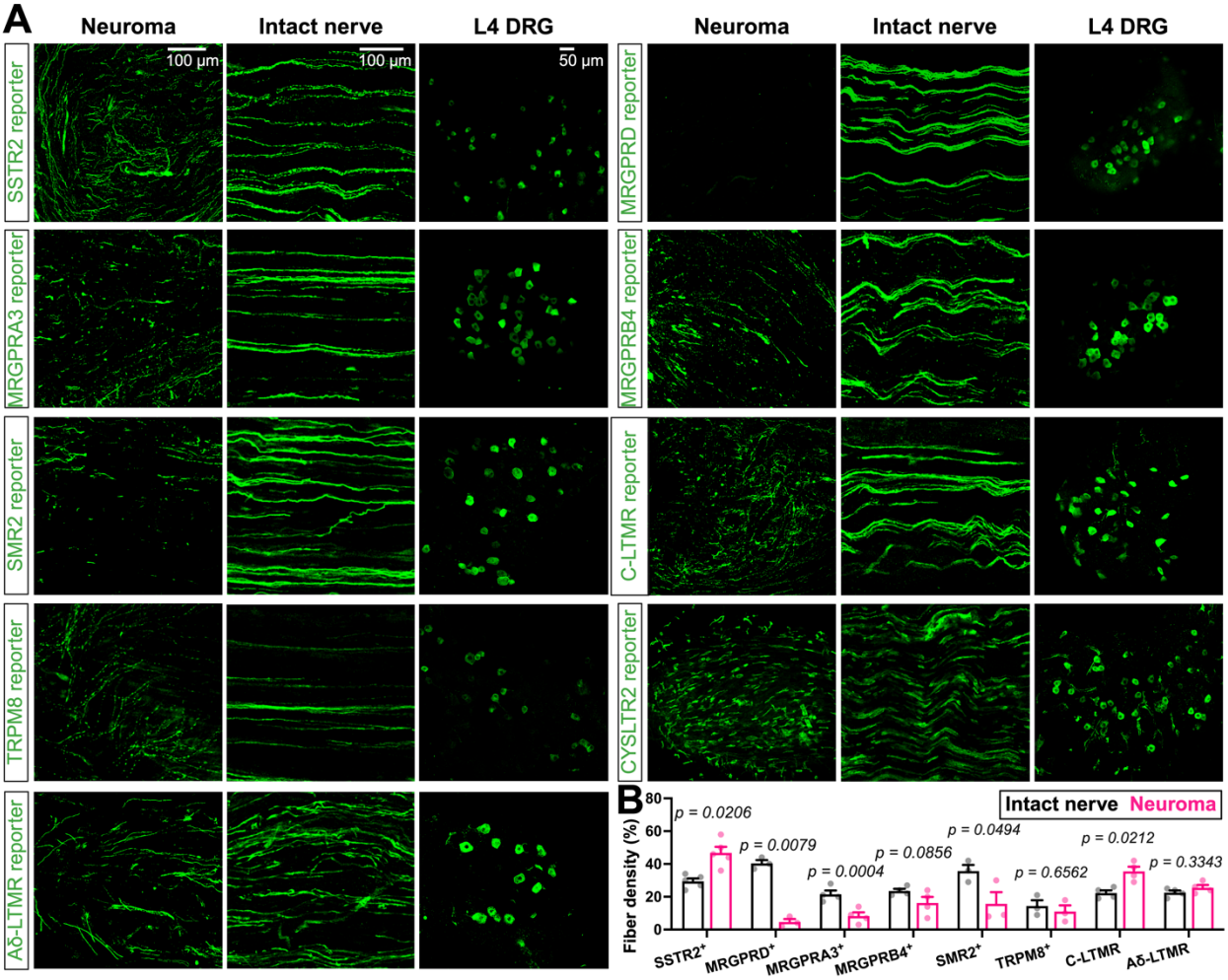

Fig. S8. Differential density of sensory fiber subtypes in neuromas. (**A**) Representative images of reporter expression (ReaChR::mCitrine) in neuromas, contralateral intact nerves, and L4 DRG neurons from transgenic lines, including SSTR2$^+$, MRGPRD$^+$, MRGPRA3$^+$, MRGPRB4$^+$, SMR2$^+$, TRPM8$^+$, C-LTMR, and Aδ-LTMRs. (**B**) Quantification of fiber density, expressed as the percentage of axon-occupied area. Note that the increased density in neuromas labeled by the C-LTMR reporter may reflect contributions from both C-LTMRs and Th$^+$ sympathetic nerves. CYSLTR2$^+$ fibers were not quantified because the transgenic line (*Cysltr2*^{Cre}) labels a mixture of axons and non-neuronal cells in peripheral nerves. Data are mean ± SEM; each dot represents one nerve/neuroma. P values from two-sided paired t-tests are shown for each population. All

these histology studies were performed following the optogenetic activation experiments at 8–12 weeks post-SNT.